

Out-of-plane shaketable testing of unreinforced masonry walls in two-way bending

Jaroslav Vaculik¹  · Michael C. Griffith¹

Received: 4 January 2017 / Accepted: 26 November 2017 / Published online: 6 December 2017
© Springer Science+Business Media B.V., part of Springer Nature 2017

Abstract Five half-scale unreinforced clay brick walls were subjected to out-of-plane shaketable testing, in order to verify whether wall behaviour observed in a previous test campaign involving quasistatic cyclic loading of full-scale walls could be considered representative under dynamic loading. The walls tested in the present study all had identical dimensions and support conditions which included translational support at their top and bottom edges and fixed support at their vertical edges. Three of these walls contained a window opening, and three were subjected to vertical precompression. An extensive number of individual runs were performed on every wall, comprising three basic types of input motion: pulses, harmonic excitation and realistic earthquake motions. The tests confirmed the main behavioural trends observed in the quasistatic cyclic test study, including attainment of a peak load capacity during the initial sequence of cracking, good post-cracking strength, substantial hysteretic energy dissipation, degradation of strength and stiffness with increasing size and number of cycles, and agreement between the overall cracking patterns. A discussion of the observed behaviour is provided by considering similarities and, where observed, the differences between the two studies and also between the five walls tested in the present study. As a means of standardising comparisons of key features of the measured force–displacement response of the half-scale shaketable test walls versus the full-scale cyclic test walls, theoretical predictions of ultimate strength and post-cracking strength are undertaken using simplified analytical methods utilising idealised collapse mechanisms. Predictions of the ultimate strength which allow for the tensile bond strength of the masonry show good correlation with the results of both test studies. The predicted post-cracking strength envelope is shown to be conservative within the range of deformations achieved in both sets of tests.

✉ Jaroslav Vaculik
jaroslav.vaculik@adelaide.edu.au

¹ School of Civil, Environmental and Mining Engineering, The University of Adelaide, Adelaide, SA 5005, Australia

Keywords Experimental testing · Shaketable · Unreinforced masonry · Walls · Two-way bending · Out-of-plane

1 Introduction

Local out-of-plane collapse of masonry walls is recognised as one of the main vulnerabilities of modern and historical unreinforced masonry (URM) construction under seismic loading, as evidenced through numerous catastrophic earthquake events (Page 1992; Oyarzo-Vera et al. 2009; D’Ayala and Paganoni 2011; Moon et al. 2014; Penna et al. 2014). This topic has thereby attracted a vast volume of research and generated a large body of experimental work. However, due to the diversity of possible URM materials, wall geometries, support conditions, and building interaction effects, some commonly-encountered wall configurations have not yet been adequately investigated experimentally. One such example and the focus of this paper is two-way spanning walls built with stretcher-bond unreinforced clay brick masonry—a form of construction prevalent in seismically active zones including Australia, New Zealand and parts of Europe.

The majority of previous shaketable tests investigating out-of-plane response of URM panels have focused on vertically spanning walls. This includes tests on standalone walls (Ewing and Kariotis 1981; Paquette et al. 2001; Dafnis et al. 2002; Reneckis et al. 2004; Griffith et al. 2004; Meisl et al. 2007; Derakhshan et al. 2013; Graziotti et al. 2016; Penner and Elwood 2016) as well as walls within complete buildings (Beyer et al. 2015). Among the consistent outcomes demonstrated by these studies is that vertically spanning wall panels undergo rocking behaviour and do not become destabilised unless they exceed their displacement capacity which is in the order of the wall thickness.

Two-way spanning walls—which includes any wall supported along at least one horizontal edge and one vertical edge—have received comparatively limited attention even though such support conditions are commonly encountered. This can be partly explained by the fact that it is conservative in seismic assessment to ignore any vertical supports and treat a wall as vertically spanning. However, since vertical edge supports act to enhance the ultimate flexural capacity (e.g. Lawrence and Marshall 2000; Griffith and Vaculik 2007), post-cracking load capacity (de Felice and Giannini 2001; D’Ayala and Speranza 2003; Portioli et al. 2013; Vaculik et al. 2014), as well as displacement capacity (Lagomarsino 2015; Vaculik and Griffith 2017a), ignoring the benefits of two-way action can lead to uneconomical design solutions.

An important consideration with respect to the post-cracking behaviour of two-way spanning walls is whether the main panel can remain sufficiently engaged to its return walls to facilitate the continuation of two-way action. This is in turn influenced by the shape of overall cracking pattern, degree of interlock along vertical cracks, and the relative strength of the masonry units versus bond strength (Vaculik and Griffith 2017b). In masonry where the flexural strength of the units is low compared to the strength of the bond, vertical edge cracks will tend to form cracking predominantly through the units, which can lead to separation of the façade from its returns. If separation does occur, then depending on the location of the vertical cracks, the panel can continue to respond either by normal (two-sided) rocking or one-sided rocking. This latter condition was observed in shaketable tests on heritage stone masonry by Costa et al. (2013) and specifically studied in shaketable tests by Al Shawa et al. (2012). In the alternate case in which the strength of the masonry bond is weak relative to the units, vertical edge cracks can retain some degree of frictional interlock thus enabling the continuation of two-way response in the post-cracking

state. Such behaviour has been observed throughout cyclic tests on clay brick masonry (Griffith et al. 2007), cyclic tests on heritage stone masonry (Costa et al. 2012), as well as monotonic and shaketable tests on dry-stack masonry built without mortar (D’Ayala and Shi 2011; Restrepo Vélez et al. 2014).

Additionally to the aforementioned tests, numerous shaketable studies have been undertaken in which two-way spanning panels were present as part of tests on overall buildings: Benedetti et al. (1998) undertook an extensive study on 24 half-scale, two-storey masonry buildings built with brick (English-bonded) as well as stone material; Bothara et al. (2010) tested a half-scale, two-storey, clay brick (stretcher bond) masonry building; Lourenço et al. (2013) tested two half-scale, two-storey buildings built with modern concrete blockwork; and Magenes et al. (2014) tested a pair of full-scale, two-storey heritage stone masonry buildings both with and without strengthening measures.

In previous work by the authors, eight full-scale, two-way spanning walls were subjected to cyclic testing using quasistatic displacement-controlled loading, which led to the characterisation of the walls’ cyclic force–displacement (F - Δ) behaviour (Griffith et al. 2007). The tested walls were 4000 mm and 2500 mm long, and 2500 mm tall, and each was built as a single leaf using $230 \times 110 \times 76$ mm clay brick units (length \times thickness \times height) and 10 mm thick mortar joints in a half-overlap stretcher bond pattern. Each specimen was provided with transverse return walls at the vertical edges, and was restrained using boundary conditions that included translational restraint along the top and bottom edges and combined rotational and translational restraint along the vertical edges [n.b. One of the walls was left unsupported along its top edge]. In addition, four of the walls were subjected to vertical precompression. Cyclic loading was administered in displacement control using inflatable airbags on both sides of the wall, and the applied loading history comprised increasing displacement cycles until the displacement amplitude approached the wall thickness of 110 mm.

The quasistatic cyclic tests demonstrated that even after the walls became fully cracked, the vertical supports remained active and the walls continued to exhibit two-way action. The associated F - Δ behaviour (refer Fig. 17 in “Appendix 2”) displayed favourable characteristics with respect to seismic performance, including substantial post-peak strength, a large displacement capacity that exceeded the instability displacement of vertically spanning walls (i.e. $>$ wall thickness), and hysteretic energy dissipation from activation of internal friction mechanisms. The walls however also underwent strength and stiffness degradation, and asymmetric behaviour when they were loaded toward and away from their return walls. Nonetheless, despite the generally favourable observations, an inherent aspect of the test arrangement was that the airbags may have acted to artificially confine the test panels thus leading to better apparent performance than under true dynamic loading—thereby necessitating the validation of the observed trends through shaketable testing.

This paper reports a study in which five two-way spanning URM walls were tested on a shaketable. The test specimens were half-scale replicas of the full-scale walls from the original quasistatic cyclic tests (Griffith et al. 2007), each with identical dimensions and support conditions that included translational restraint along all four edges together with moment restraint along the vertical edges. An overarching objective of this study was to verify whether the wall behaviour observed in the quasistatic cyclic tests could be considered representative under true dynamic loading. The test results are also used for comparison to theoretical predictions of ultimate residual and residual strength capacities. Furthermore, the data generated could be used in the future development of a time-history

analysis. These data are made publicly available as part of the Supplementary Material provided with this paper (available online).

2 Experimental test programme

2.1 Materials

To meet laboratory capabilities, the test walls were built as half-scale versions of the walls in the original quasistatic cyclic test study (Griffith et al. 2007). The masonry units used were solid clay bricks with nominal dimensions $110 \times 50 \times 39$ mm (length, width, height). Mortar joints were made to a nominal thickness of 5 mm using a 1:2:9 mix (Portland cement: lime: sand). All test specimens including the five test walls and material test specimens were constructed by qualified bricklayers under controlled laboratory conditions. To ensure consistency in the mortar, ingredients were measured by bucket batching, and sand was air-dried prior to mixing. Water was gradually added to the mix within a mixer to achieve appropriate workability based on the bricklayers' experience.

To quantify values of key mechanical properties, a series of material tests were conducted on small specimens constructed using the same materials as the test walls. These tests were performed in accordance with guidelines in the Australian masonry standard AS 3700 (Standards Australia 2011). The associated test procedures and detailed results are reported in the Supplementary Material provided with this paper (“Appendix 1”). Mean values of the properties as well as their coefficients of variation (COV = ratio of the standard deviation to the mean) are provided in Table 1.

2.2 Wall configurations

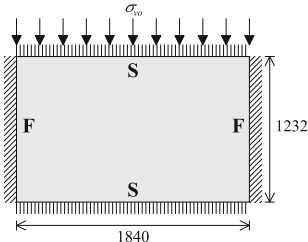
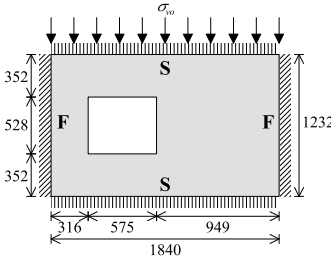
Configurations of the five walls are summarised in Table 2. Each wall comprised a single leaf built in half-overlap stretcher bond. Each wall had dimensions of 1840×1232 mm (L \times H) as shown in Fig. 1. For the purpose of stabilising the panels against overturning and implementing rotational restraint (described later), 230 mm long (2 bricks long) return walls were built into the vertical edges of the main panels using half-overlap bond.

Walls D1 and D2 were solid (without openings) and subjected to a precompression of 0.10 MPa and 0 MPa, respectively. Walls D3, D4 and D5 each contained an eccentrically positioned 676×528 mm (L \times H) window opening and were subjected to 0.10, 0.05 and

Table 1 Material properties of the masonry

Property	Symbol	Mean	COV
Flexural tensile strength of the masonry	f_{mt}	0.415 MPa	0.53
Modulus of elasticity of the masonry	E_m	9180 MPa	0.15
Modulus of elasticity of the brick units	E_u	32,100 MPa	0.16
Modulus of elasticity of the mortar joints	E_j	1410 MPa	0.20
Unconfined compressive strength of the masonry	f_{mc}	25.9 MPa	0.09
Friction coefficient across bond interface	μ_m	0.576	0.10
Weight density of masonry	γ	21.2 kN/m ³	–

Table 2 Test wall configurations

Panel dimensions (mm) and support arrangement	Wall	Precompression, σ_{vo} (MPa)
	D1	0.10
	D2	0
	D3	0.10
	D4	0.05
	D5	0

F fixed support, *S* simple support

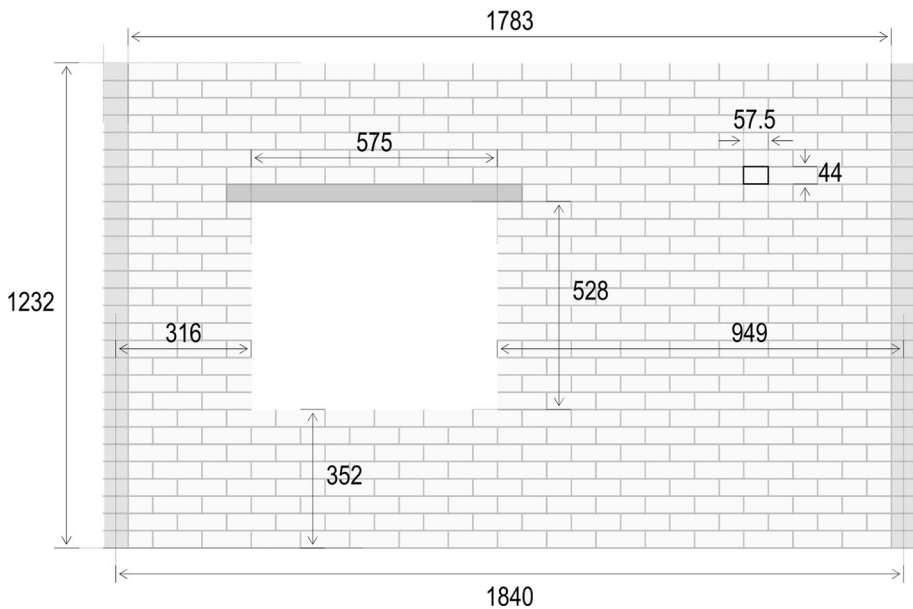


Fig. 1 Wall dimensions (in millimetres). Note that window opening is present only in walls D3–D5 (absent in D1 and D2)

0 MPa precompression, respectively. The window was formed using a 50 × 5 mm equal angle steel lintel. Each wall was constructed on a concrete slab which enabled it to be lifted onto the shaketable for testing.

2.3 Support conditions

Wall edge support conditions were intended to replicate as close as possible those used in the quasistatic cyclic tests (Griffith et al. 2007) by using the same methods of restraint. The applied boundary conditions were kept identical for each of the five walls, whereby the top and bottom edges were restrained against lateral displacement (pinned support), and both vertical edges were restrained against lateral displacement and rotation (fixed support). The restraint system utilised a support frame consisting of a pair of diagonally-braced steel diaphragms at each end of the wall, whose in-plane stiffness was intended to be comparable to that of in-plane URM walls.

2.3.1 Bottom edge

Despite the presence of a base mortar joint, additional restraint was provided to prevent possible sliding between the wall and supporting slab and ensure translational support. This was achieved using steel walers on each side of the wall as shown by Figs. 2 and 3a. Due to the established view that moment capacity along horizontal cracks is negligible toward walls in two-way bending (e.g., Lawrence and Marshall 2000), the support condition along the bottom edge can be considered to be pinned.

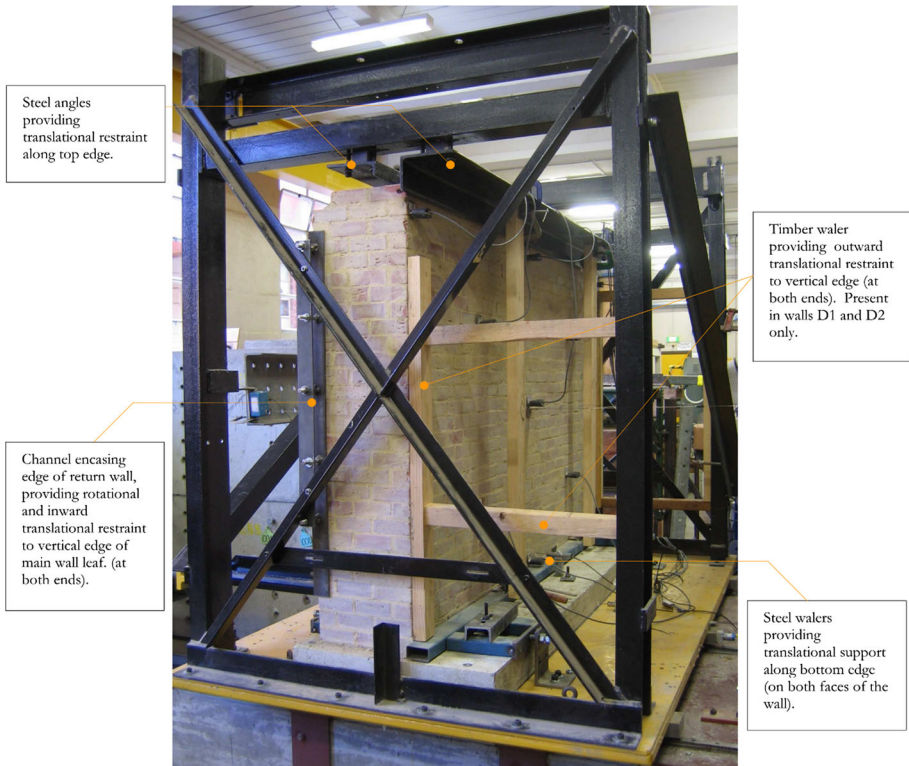


Fig. 2 Photograph showing various aspects of the restraint system. Wall D2 shown

2.3.2 Top edge

Translational restraint along the top edge was achieved using steel angles placed adjacent to each side of the wall, as shown in Figs. 2 and 3a. Lateral contact between the angles and the wall was made across rubber bearings to encourage a more uniform distribution of the reaction force. As the top edge was allowed to rotate, the overall restraint can be considered as pinned.

The supporting angles in turn spanned between the in-plane steel frames and had sufficient bending stiffness to minimise deflection under loading and mimic a stiff top diaphragm. In the majority of test runs performed, the combined stiffness of the restraint system was sufficient to limit the relative deflection between the centre of the top support and the table (i.e. interstorey drift) to less than 2 mm and a maximum recorded value of 5 mm. It should be noted that the top edge restraint system implemented in the quasistatic cyclic tests (Griffith et al. 2007) was comparatively stiffer than in the present study and limited deflections to values that can be deemed negligible.

2.3.3 Vertical edges

The restraint system used to impose moment connections along the vertical edges is illustrated in Figs. 2 and 3a. It comprised two components: The first was a steel channel that encased the free vertical edge of the return wall. This prevented lateral displacement of the return and thus restrained the vertical edges of the main wall face against rotation regardless of loading direction, as well as against translation under inward loading. This system was implemented on every wall and was identical to that used in the quasistatic cyclic tests.

Secondly, a vertical timber waler was used to prop the outside face of the return wall, to provide a more effective form of translational restraint along the vertical edge under outward loading. This restraint was only used on walls D1 and D2 in order to prevent rigid body rocking of the entire specimen (main panel plus returns) about the base, which was observed while testing wall D2 (n.b. In wall D2, this restraint was implemented from run 20 onwards). This form of restraint was not implemented the quasistatic tests as it was not considered necessary.

2.4 Vertical precompression

Three of the test walls were subjected to vertical precompression, including wall D1 (0.10 MPa), D3 (0.10 MPa) and D4 (0.05 MPa). The apparatus used to impose the precompression, shown in Fig. 4, consisted of four pairs of post-tensioned springs with steel rods anchored to the table. Each pair of rods was fixed to a steel angle which transferred the compressive reaction back to the wall via a square bar, timber plate, and a rubber packer. This arrangement was consistent with that used in the quasistatic cyclic tests and ensured that the applied load was concentric and uniform. The target level of precompression was controlled by adjusting the extension of the springs to a pre-calibrated deflection. The springs were designed to operate at large extension, so that small changes in the height of the wall due to rigid body rotation would result in minimal influence on the precompression.

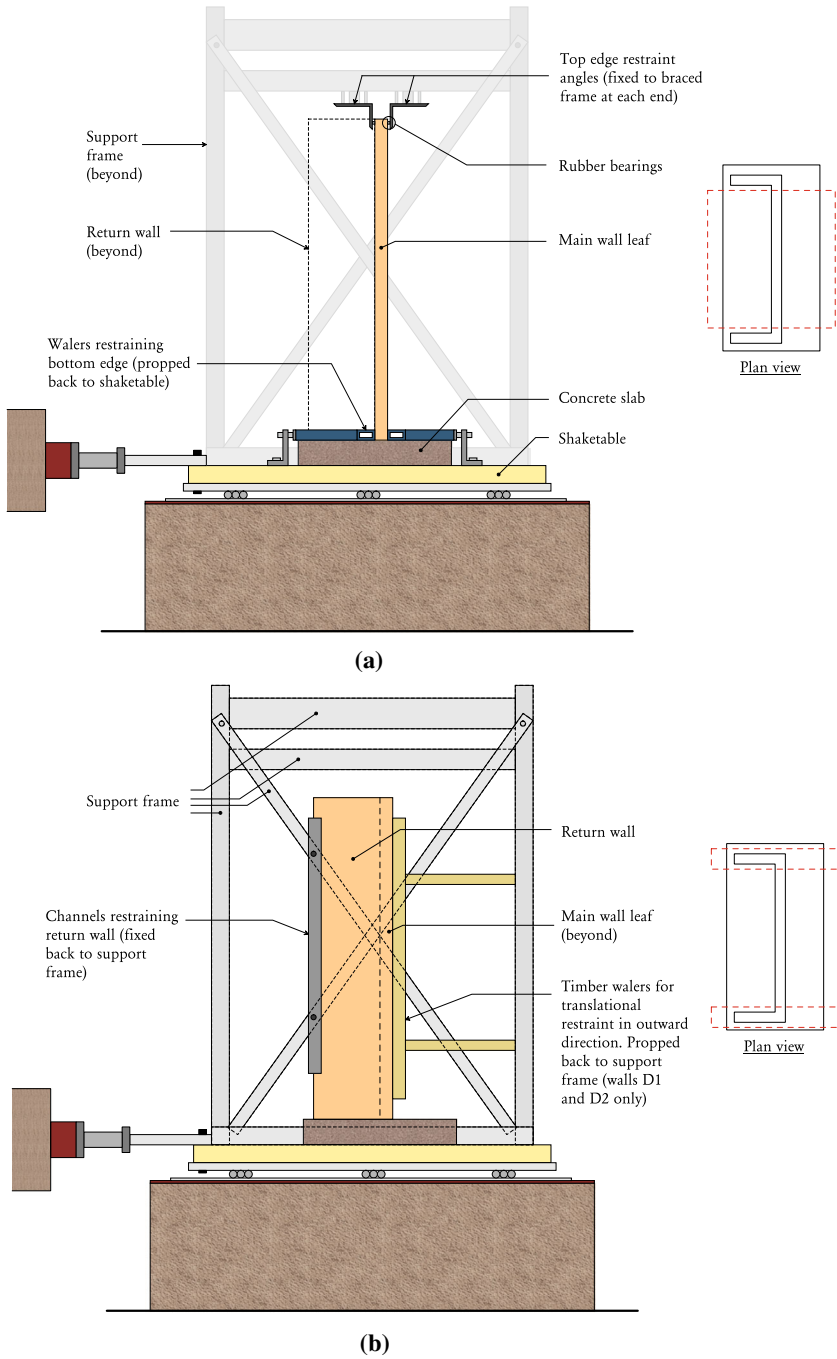


Fig. 3 Arrangements used to restrain the wall’s edges. **a** Restraint along top and bottom edges, **b** restraint along vertical edges

It should be noted that the quasistatic cyclic tests used a system of cantilevered weights instead of post-tensioned springs to generate the precompression load; however, the resulting effect on wall behaviour is thought to be negligible.

2.5 Test procedure

Whilst the overall test run sequence differed between each wall, the general testing strategy was kept consistent and performed in two stages. Firstly, the as-yet uncracked wall was subjected to a free vibration pulse test to determine its natural frequency. Harmonic motions were then run at the wall's natural frequency at increasing intensity until the wall cracked and a failure mechanism was established. The second phase of testing was then performed, in which the wall was subjected to a series of earthquake motions at increasing intensity. Free vibration tests were conducted regularly to quantify any changes to the wall's natural frequency as a result of damage accumulation.

Over the course of testing, each wall was subjected to a large number of individual test runs (ranging between approx. 60–120) comprising three basic types of table input motions:

2.5.1 Pulse tests

In these tests, the table input motion was a displacement step function, stepping from $x = 0$ to x_o at constant velocity over a predefined time step. Two pulses were applied in each run: one forward (0 to x_o) and one backward (x_o to 0). The role of these tests was to induce free vibration response of the wall. Each pulse test comprised three runs at increasing intensity: 4 mm over 0.2 s, 4 mm over 0.1 s and 8 mm over 0.1 s.

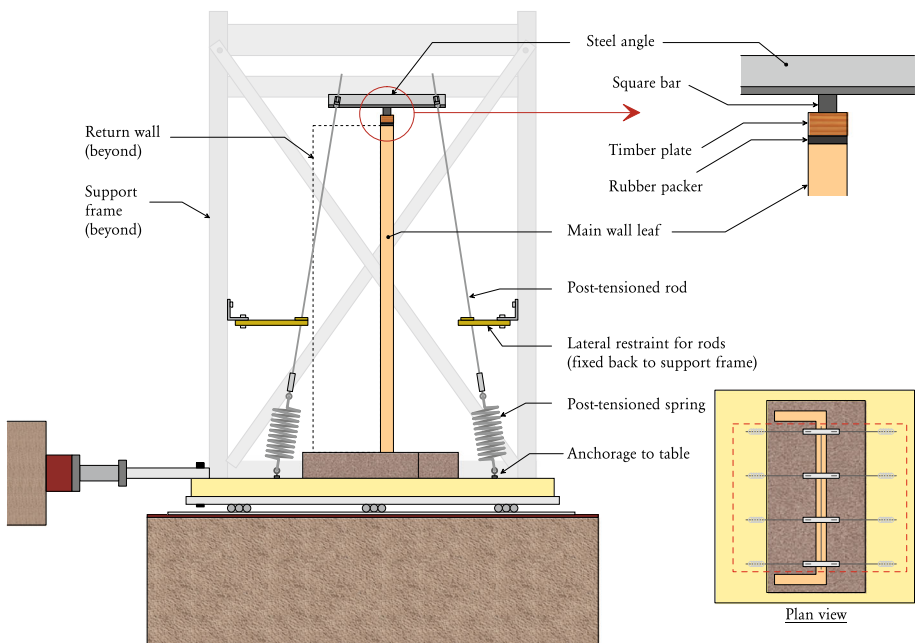


Fig. 4 Arrangement used to apply vertical precompression

2.5.2 Harmonic tests

These tests used sinusoidal input motion at a constant excitation frequency. Each run consisted of three phases: ramp-up (typically 2 s), constant amplitude (typ. 6 s) and ramp-down (typ. 2 s). The main objective of harmonic motions was to cause the wall to crack in the early stages of testing; however, they were also run at later stages in order to generate symmetric cyclic loading.

2.5.3 Earthquake tests

These tests involved earthquake-like motions with a broad frequency content. The main motion used was the 1952 Kern County ‘Taft’ record sped up by a factor of $\sqrt{2}$ to preserve frequency similitude in the half-scale specimens. Several synthetically generated motions were also used. In the overall test sequence, earthquake tests were run as pairs at equal magnitude but alternating directionality, in order to discourage directional bias due to motion asymmetry. For example, a run with a peak ground displacement (PGD) of + 60 mm was followed by a run with PGD of – 60 mm.

Further detail regarding basic input motions and test run sequences is provided in the Supplementary Material (“[Appendix 1](#)”).

2.6 Scaling effects and similitude

Due to laboratory limitations it was impractical to provide full dynamic similitude between the tested half-scale walls and full-scale prototypes as this would have required increasing the material density of the masonry. It is emphasised however that the intention of these tests was to provide a qualitative rather than quantitative comparison of wall behaviour with the quasistatic cyclic tests reported in Griffith et al. (2007), and thus the adopted testing approach is considered to be valid. Furthermore, the theoretical predictions made later in this paper (Sect. 5) inherently account for these scaling effects.

2.7 Comparison of the dynamic and quasistatic cyclic testing approaches

Since one of the main motivations of undertaking these shaketable tests was to validate the behaviour observed in the quasistatic cyclic tests (Griffith et al. 2007), it is important to briefly consider some of the fundamental aspects of the testing approaches.

The main benefit of quasistatic cyclic testing is that it enabled the out-of-plane F- Δ behaviour to be studied under precisely controlled displacement histories. This in turn allowed for straightforward quantification of effects such as strength and stiffness degradation, as well as hysteretic damping.

Quasistatic testing however requires an initial assumption regarding the shape of the imposed load pattern. In the previous quasistatic tests loading was administered using airbags which generated an approximately uniform load along the face of the wall. By contrast, during seismic response the wall experiences inertia-proportional loading whose spatial distribution is in turn dependent on the mode shape, which means that the wall’s mass is not mobilised exactly uniformly. However, whilst the uniform loading applied in the quasistatic tests was an approximation, it is deemed to be acceptable one in the context of studying the F- Δ behaviour.

Other relative merits of the different testing methods with respect to URM structures have already been well discussed by others (e.g. Calvi et al. 1996; Abrams 1996). However it should be noted that quasistatic cyclic tests are generally regarded to provide a lower-bound representation of expected strength under dynamic loading, due to rate-dependency of crack propagation, and the fact that displacement histories used in quasistatic cyclic tests tend to be more severe than random earthquake motions in terms of the quantity of imposed cycles. In the present tests, however, the imposed displacement histories are deemed to be relatively punishing due to the large number of test runs performed on each wall.

3 Data processing

Each wall was fitted with an array of instrumentation comprising 10 accelerometers and 6 displacement transducers. The acquired data were then processed in two stages. Firstly, the raw displacement and acceleration data were used to compute the time-domain force (F) and displacement (Δ) response of the wall. Secondly, the wall's F - Δ time trace was used to quantify key cyclic properties including effective stiffness, damping and vibrational frequency. These processes will now be briefly discussed, with further description provided in the Supplementary Material (“Appendix 1”).

3.1 Time-domain response

The following notation is adopted in the upcoming discussion: x = position measured with respect to stationary reference frame; Δ = wall displacement relative to its supports; a = acceleration.

3.1.1 Wall displacement

The reference position of the wall's supports ($x_{\text{sup.avg}}$) was taken as the average of positions of the top and bottom supports ($x_{\text{sup.bot}}$ and $x_{\text{sup.top}}$), such that:

$$x_{\text{sup.avg}} = 0.5(x_{\text{sup.bot}} + x_{\text{sup.top}}). \quad (1)$$

The wall's central displacement was computed as the position of the wall's centre relative to the supports:

$$\Delta_c = x_{\text{w.cent}} - x_{\text{sup.avg}}, \quad (2)$$

where a positive displacement denotes displacement toward the return walls.

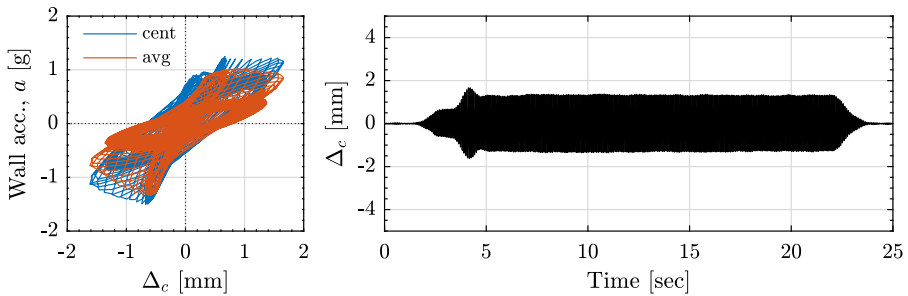
In interpretation of the test results it is convenient to consider the wall's displacement normalised by the wall thickness ($t_u = 50$ mm), which is denoted by δ :

$$\delta = \Delta/t_u. \quad (3)$$

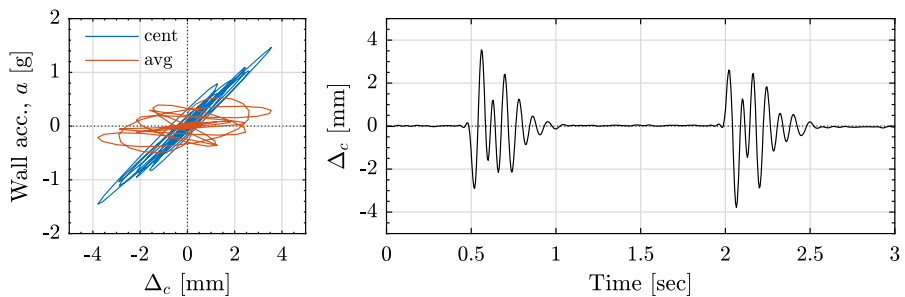
3.1.2 Wall acceleration and force resistance

Two alternate measures of the wall's acceleration are used in the interpretation of the results: central acceleration, $a_{\text{w.cent}}$, measured directly by an accelerometer located at the

(a) Test run d2.13_H_12Hz_0.25mm



(b) Test run d2.32_R_8mm_100ms



(c) Test run d2.41_EQ_Taft_-100mm

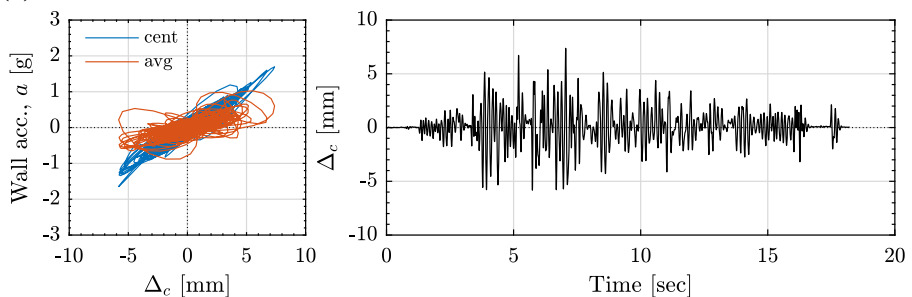


Fig. 5 Examples of typical wall response including central and average wall acceleration versus central displacement (left) and central displacement versus time (right). Shown for **a** harmonic test, **b** pulse test, and **c** earthquake motion test

centre of the wall; and average acceleration, $a_{w,avg}$, calculated as a weighted average of numerous accelerometers positioned along the wall.

From the equation of motion it follows that if velocity-proportional damping forces are assumed to be negligible, then the force resisted by the wall becomes directly proportional to the wall’s average acceleration, as per the equation:

$$F_w = -M_w a_{w,avg}, \tag{4}$$

where M_w is the mass of the wall:

$$M_w = \gamma t_u A_w / g, \tag{5}$$

where γ is the weight density of the wall, A_w is the wall’s net area, and g is gravitational acceleration. Following from Eq. (4), the average wall acceleration may be used interchangeably as a measure of the wall’s load resistance, however noting the following points.

Examination of the test data revealed that the central acceleration (as opposed to the average acceleration) provided the more reliable representation of the wall’s fundamental ‘flexural’ mode of vibration. This was evidenced by the fact that the central acceleration produced cleaner hysteresis loops when plotted versus the central displacement, as well as examination of the respective Fourier spectra which indicated that the average acceleration generally contained interference from higher vibrational modes (possibly twisting of the walls or vibration of the support frame). It is worth noting that the ratio of the peak $a_{w,cent}$ to peak $a_{w,avg}$ typically ranged between 1.5 and 4. Typical comparison of average and central acceleration in terms of generated hysteresis loops is provided in Fig. 5.

For the aforementioned reasons, the average wall acceleration was treated as a more reliable measure of the force resistance capacity (refer to Sect. 4.1), whilst the central acceleration was considered to be as a better indicator of the ‘true’ hysteresis loop shape including hysteretic damping (refer to Sect. 4.3).

3.2 Cyclic response properties

A post-processing routine was implemented on the time-domain data to derive values of key properties using the following steps:

1. A cycle detection algorithm was implemented to find individual cycles in the wall’s displacement response.
2. Properties of interest including a and Δ amplitudes, secant stiffness, damping and frequency were computed for each cycle, as described below.
3. Average values of the properties were calculated for specific ranges of displacement response, including small and large displacement.

The following properties were computed for individual cycles, as illustrated by Fig. 6.

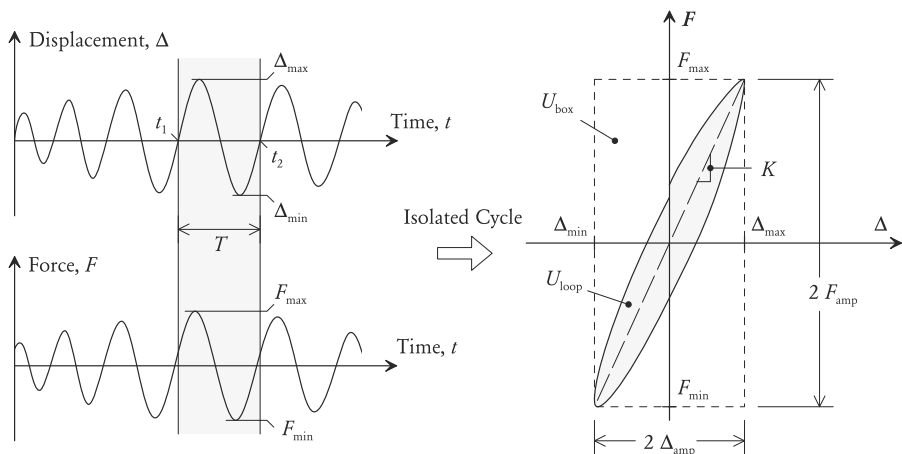


Fig. 6 Hysteresis loop for an isolated cycle and the properties derived

3.2.1 Displacement amplitude

To account for the fact that response cycles were not necessarily centred about $\Delta = 0$, the displacement of the cycle was quantified in terms of its amplitude, as follows:

$$\Delta_{\text{amp}} = \frac{1}{2}(\Delta_{\text{max}} - \Delta_{\text{min}}), \quad (6)$$

where Δ_{max} and Δ_{min} are the largest displacement excursions in a cycle.

3.2.2 Acceleration and force amplitude

Similarly, the amplitude of the average or central acceleration was calculated as

$$a_{\text{amp}} = \frac{1}{2}(a_{\text{max}} - a_{\text{min}}). \quad (7)$$

The amplitude of force resistance (F_{amp}) was computed from the average acceleration amplitude using Eq. (4).

3.2.3 Secant stiffness

The secant stiffness (K) was obtained as

$$K = F_{\text{amp}}/\Delta_{\text{amp}}. \quad (8)$$

3.2.4 Hysteretic damping

Hysteretic damping was quantified in terms of equivalent viscous damping ratio (ξ) using the expression

$$\xi = \frac{2 U_{\text{loop}}}{\pi U_{\text{box}}}, \quad (9)$$

where U_{loop} is the energy dissipated during the cycle (area enclosed by the hysteresis loop), and U_{box} is the area inside the loop's bounding box which is proportional to the internal strain energy of an equivalent linear system. For reasons discussed in Sect. 3.1.2, ξ was computed on the basis of central wall acceleration.

3.2.5 Free vibration period

To estimate the wall's free vibration period (T), the duration of individual cycles was quantified from the displacement response waveform using the data recorded from pulse tests and earthquake motion tests. The corresponding frequency was calculated as $f = 1/T$.

For every test run performed, average values of the aforementioned properties (Δ and a amplitudes, K , ξ , and T) were computed within the following ranges of displacement:

- *Small displacement range*, which incorporated cycles whose Δ_{amp} was within 0.5 and 3.0 mm. This was intended to capture the response along the initial loading branch of the F - Δ curve; and
- *Peak displacement response range*, which incorporated all cycles whose displacement amplitude was within 70 to 100% of the largest Δ_{amp} occurring in the test run.

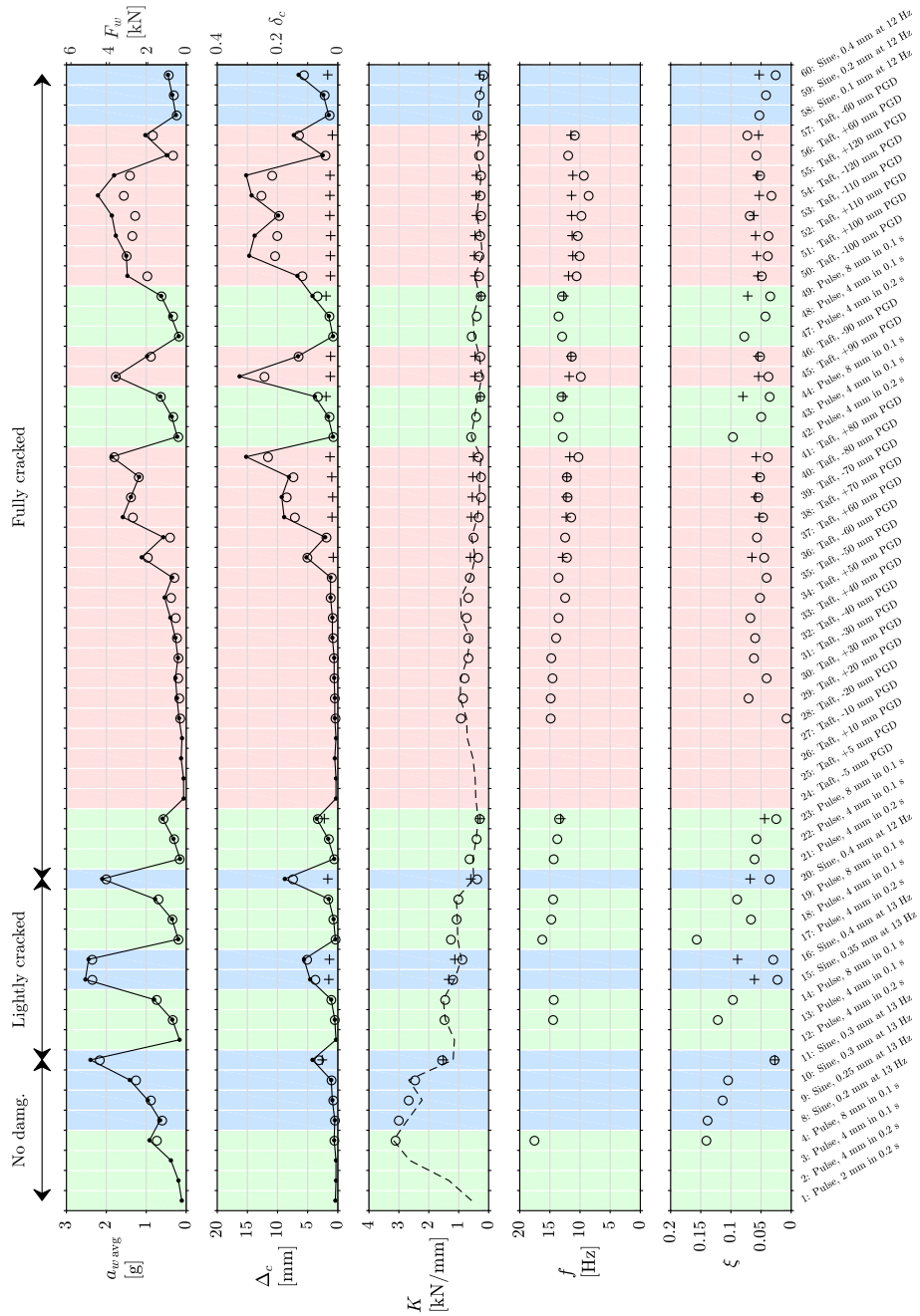


Fig. 7 Test sequence and key results for wall D3

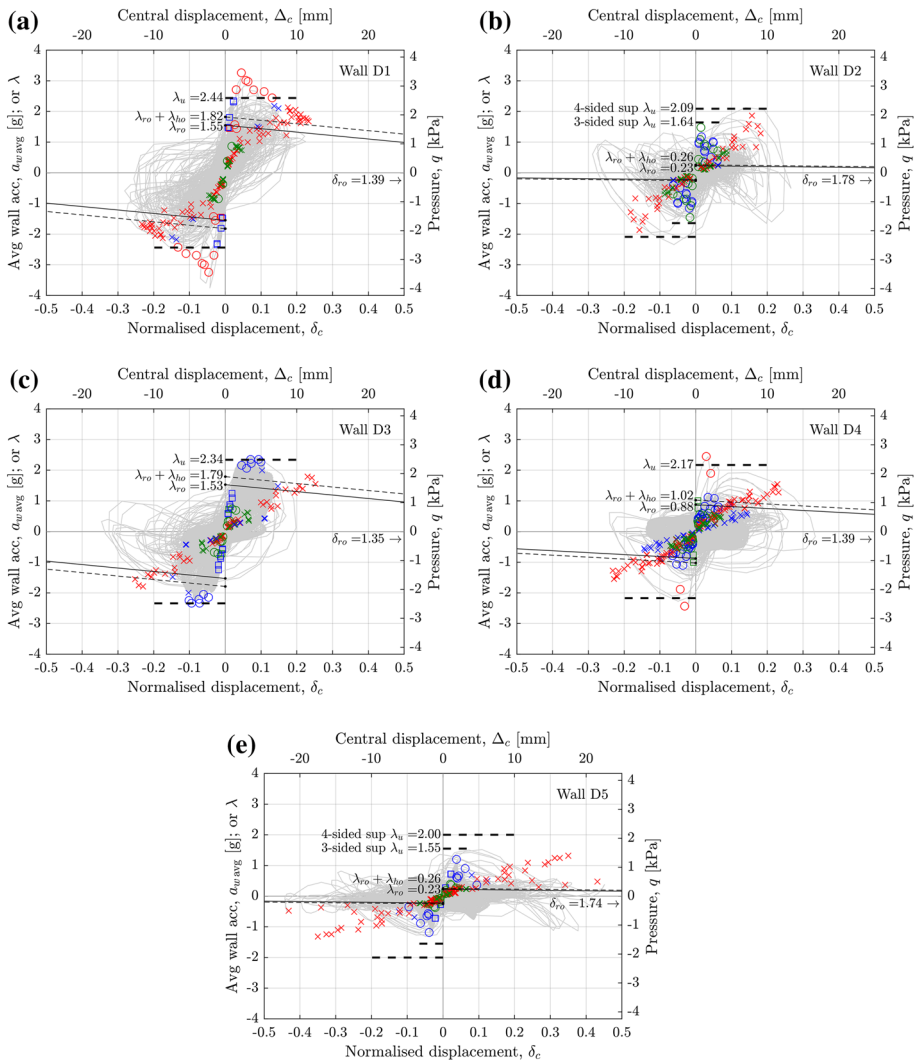





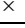


Fig. 8 Capacity curves of average wall acceleration versus central displacement. Grey ‘cloud’ superimposes data from all test runs undertaken. Markers (circle, square, cross) indicate the largest amplitude cycles identified in each test run (legend provided in Table 3). Superimposed onto the experimental plots are analytical capacity predictions including: ultimate strength λ_u (thick dashed line), residual strength from rigid body rocking λ_{ro} (thin solid line, x-intercept at δ_{ro}), and residual strength inclusive of horizontal bending friction $\lambda_{ro} + \lambda_{ho}$ (thin dashed line)

It should be noted that prior to the analysis being conducted, the data were digitally filtered in the frequency domain to improve the effectiveness of the cycle detection algorithm. Data from pulse and earthquake tests were filtered using a low-pass filter with the cutoff frequency manually set between 30 and 50 Hz, depending on the initial cleanliness of the raw data. Data from harmonic tests were filtered using a comb filter passing spectral content at the first three harmonics of the excitation frequency.

Table 3 Legend for Figs. 8, 9, 10 and 11

Colour	Input motion type
	Pulse test
	Harmonic test
	Earthquake test
Marker	Wall damage state
	Uncracked
	Lightly cracked
	Fully cracked

Further details are provided in the Supplementary Material (“Appendix 1”) including a description of the filtering methods, cycle detection algorithm, graphical examples of analysis output, and summary of test results for each individual run.

4 Test results

4.1 Force–displacement response

Demonstrative examples of typical wall response in pulse, harmonic and earthquake motion tests are shown by Fig. 5 in terms of time-domain Δ response together with a - Δ hysteresis curves. A typical example of the individual test run sequence and properties derived is shown for wall D3 in Fig. 7. Plots for the remaining walls are provided within the Supplementary Material (“Appendix 1”).

Experimental F - Δ capacity curves in terms of average wall acceleration versus central displacement are provided in Fig. 8 for each wall. These plots superimpose hysteresis data measured during the entire set of tests together with markers indicating the amplitudes of the largest cycles in individual test runs. Note that the marker type denotes the damage state of the wall as either uncracked, lightly cracked (i.e. some cracking present but not full collapse mechanism), or fully cracked (i.e. having developed a full collapse mechanism) as per the legend in Table 3. Further superimposed onto these plots are analytical predictions which are discussed in Sect. 5.

Figure 9 provides a - Δ capacity curves in a manner similar to Fig. 8 but using the wall’s central acceleration instead of average acceleration, in order to further demonstrate the difference between the shapes of their hysteresis.

The most notable feature of the measured F - Δ behaviour in the present tests (through Figs. 5, 8, 9) is its irregular nature in comparison to the relatively ‘smooth’ F - Δ curves obtained in the quasistatic cyclic tests (provided in “Appendix 2”). This however is deemed to be a typical aspect of dynamic testing, whereby the greater degree of control over the imposed displacements in quasistatic testing is among its main advantages as a testing approach. Despite these differences, the general trends in F - Δ behaviour observed in the two studies are considered to be consistent, including: (a) initial cracking as well as peak strength being reached at relative small wall displacements, (b) progressive degradation of stiffness with accumulation of damage, and (c) hysteretic energy dissipation. The remainder of this section will discuss these observations in greater detail.

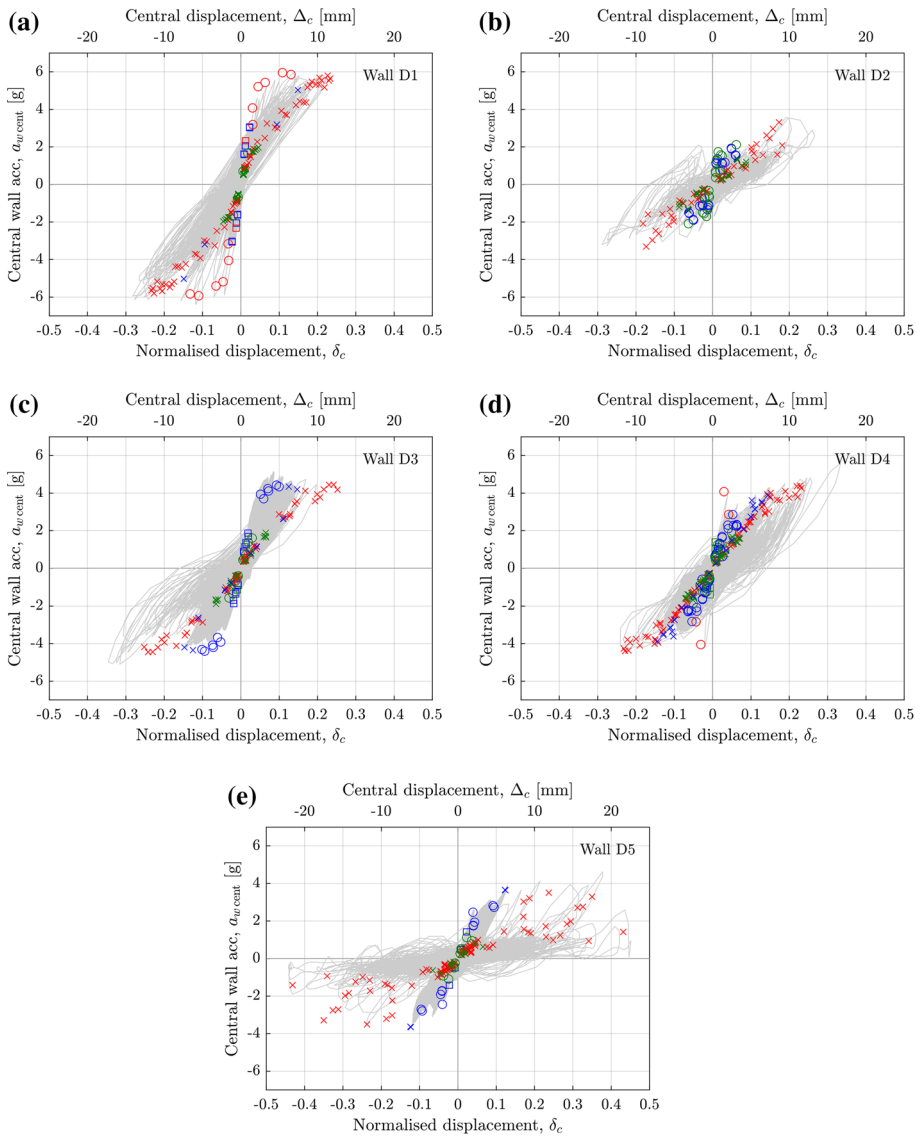


Fig. 9 Capacity curves of central wall acceleration versus central displacement. Grey ‘cloud’ superimposes data from all test runs undertaken. Markers (circle, square, cross) indicate the largest amplitude cycles identified in each test run (legend provided in Table 3)

4.1.1 General behaviour

To demonstrate typical wall response, consider the behaviour of wall D3 through the $F-\Delta$ capacity plot in Fig. 8c and test run sequence plot in Fig. 7. As shown by the $F-\Delta$ capacity plot, the response of the as-yet uncracked wall (square markers in Fig. 8) was roughly linear up to about 1 mm displacement, encompassing test runs 4, 8, 9 and 10 during which

the secant stiffness K remained approximately constant. Cracking initiated in test run 11 at $\Delta \approx 2$ mm resulting in a large reduction in secant stiffness. The wall then progressively cracked throughout test runs 11, 15 and 16 (circle markers in Fig. 8) during which it achieved its ultimate strength of 2.3 g over Δ range ≈ 2.3 –4.7 mm; this process was characterised by a further continual reduction in stiffness as seen in Fig. 7. In test run 20 the wall was now considered to be ‘fully cracked’—that is the crack pattern was sufficiently evolved to constitute a collapse mechanism (refer to Sect. 4.5).

Once fully cracked, the walls were subjected to a series of earthquake motion runs at increasing intensity with resulting F - Δ excursions indicated in Fig. 8 by cross markers. At this stage, the walls each underwent rocking type response to some degree, with opening and closure of cracks along each face. From Fig. 8 it can be seen that once a wall had become fully cracked, its stiffness was substantially reduced compared to the earlier uncracked and lightly-cracked states. Interestingly, the overall cluster of F - Δ excursions appears to form a generally linear trend up to the displacements reached in the tests, in particular for walls D2–D5. It should be noted that even once the walls became ‘fully cracked’ they still continued to accumulate further damage in the form of additional localised cracking and widening of already-formed cracks (discussed further in Sect. 4.5).

Overall trends in the F - Δ capacity response of the remaining walls are considered similar to those of wall D3, although a notable feature of the capacity curves in Fig. 8 is that walls D1, D3 and D4 (walls with precompression) achieved their global peak load during the cracking phase. By contrast, walls D2 and D5 (walls without precompression) achieved an initial local peak in the cracking phase, but their global maximum load was reached in later test runs once the wall was fully cracked. This is thought to be due the top support connection being less effective at small displacements in tests on wall D2 and D5 which is supported by the observed crack patterns (Sect. 4.5) and also comparisons to analytical predictions (Sect. 5).

4.1.2 Strength and stiffness degradation

As observed through the a - Δ plots in Figs. 8 and 9 each wall experienced strength and stiffness degradation as it was subjected to increasing levels of deformation and number of cycles during the course of testing. This trend is also evident from Fig. 7 through a continual reduction in secant stiffness accompanied by a reduction in vibrational frequency (discussed further in Sect. 4.4). Although it is not possible to quantitatively compare the rate of cycle-to-cycle degradation in these tests to the quasistatic cyclic tests due to the difference in loading histories, the presence of strength and stiffness degradation is a consistent feature of both two studies.

The observed degradation was symptomatic of the accumulation of damage as a result of the following:

- Progressive tensile and shear cracking of the brick to mortar bond;
- Localised crushing and spalling of bed joint mortar resulting from crack rotation; and
- Sliding between adjacent panels and widening of existing cracks, thus leading to reduced area of overlapping bedded area (e.g., refer to Fig. 13 showing wall D3).

4.1.3 Peak strength

The peak measured strength of the walls in terms of the peak acceleration amplitude observed in Fig. 8 is summarised in Table 4. Due to the presence of two distinct peaks in

Table 4 Ultimate load capacities determined as peak values from plots of average acceleration versus displacement (Fig. 8)

Wall (σ_v in brackets)	Peak a_w avg (g)	Peak F_w (kN)	Δ_c at peak (mm)	δ_c at peak	Comment
D1 (0.1 MPa)	3.25	7.81	2.3	0.05	Global peak, occurred in cracking phase
D2 (no precomp.)	1.47	3.52	0.8	0.02	First peak (local max); occurred in cracking phase
D2	(1.87)	(4.48)	(7.9)	(0.16)	Second peak (global max), occurred in fully cracked phase
D3 (0.1 MPa)	2.34	4.87	2.3–4.7	0.09	Global peak, occurred in cracking phase
D4 (0.05 MPa)	2.44	5.07	1.5	0.03	Global peak, occurred in cracking phase
D5 (no precomp.)	1.19	2.48	1.9	0.04	First peak (Local max); occurred in cracking phase
D5	(1.32)	(2.74)	(17.5)	(0.35)	Second peak (global max), occurred in fully cracked phase

In walls D1, D3 and D4 the global maximum peaks occurred during the initial cracking phase. In walls D2 and D4 the global peaks occurred in the fully cracked phase and thus the initial peak occurring in the cracking phase is reported separately

the response of walls D2 and D5, the table reports both values. It should be noted however that due to the approximately linear trend between F and Δ in the fully cracked state, the second maximum should not be regarded as a true peak but rather the force reached at the largest imposed displacement.

It is seen that each wall reached its initial peak load capacity within $\Delta \approx 1\text{--}5$ mm ($\delta \approx 0.02\text{--}0.1$). The fact that these peaks were reached at low displacement is consistent the quasistatic cyclic tests (Griffith et al. 2007) as well as airbag loading tests by Lawrence (1983). In the former, the walls had generally reached 80% of their ultimate strength at normalised displacements of $\delta \approx 0.02$ ($\Delta \approx 2$ mm) and typically maintained this load up to $\delta \approx 0.20\text{--}0.35$ ($\Delta \approx 22\text{--}38$ mm).

4.1.4 Residual strength and displacement capacity

For the purpose of comparing the post-cracking strength of the tested walls, the load resistance of the each fully cracked wall was determined from each wall's $F\text{--}\Delta$ capacity curve at a reference displacement of $\delta = 0.2$ ($\Delta = 10$ mm). These values are summarised

Table 5 Post-cracking strength measured at a reference displacement of $\delta = 0.2$ ($\Delta = 10$ mm). Values are deduced from $F\text{--}\Delta$ capacity curves (Fig. 8) as an average value for the cycle excursions near the reference displacement

Wall (σ_v in brackets)	a_w avg (at $\delta = 0.2$) [g]	Comment
D1 (0.1 MPa)	1.8	–
D2 (no precomp.)	1.5	Reference Δ not reached; value obtained by extrapolation
D3 (0.1 MPa)	1.5	–
D4 (0.05 MPa)	1.1	–
D5 (no precomp.)	0.8	–

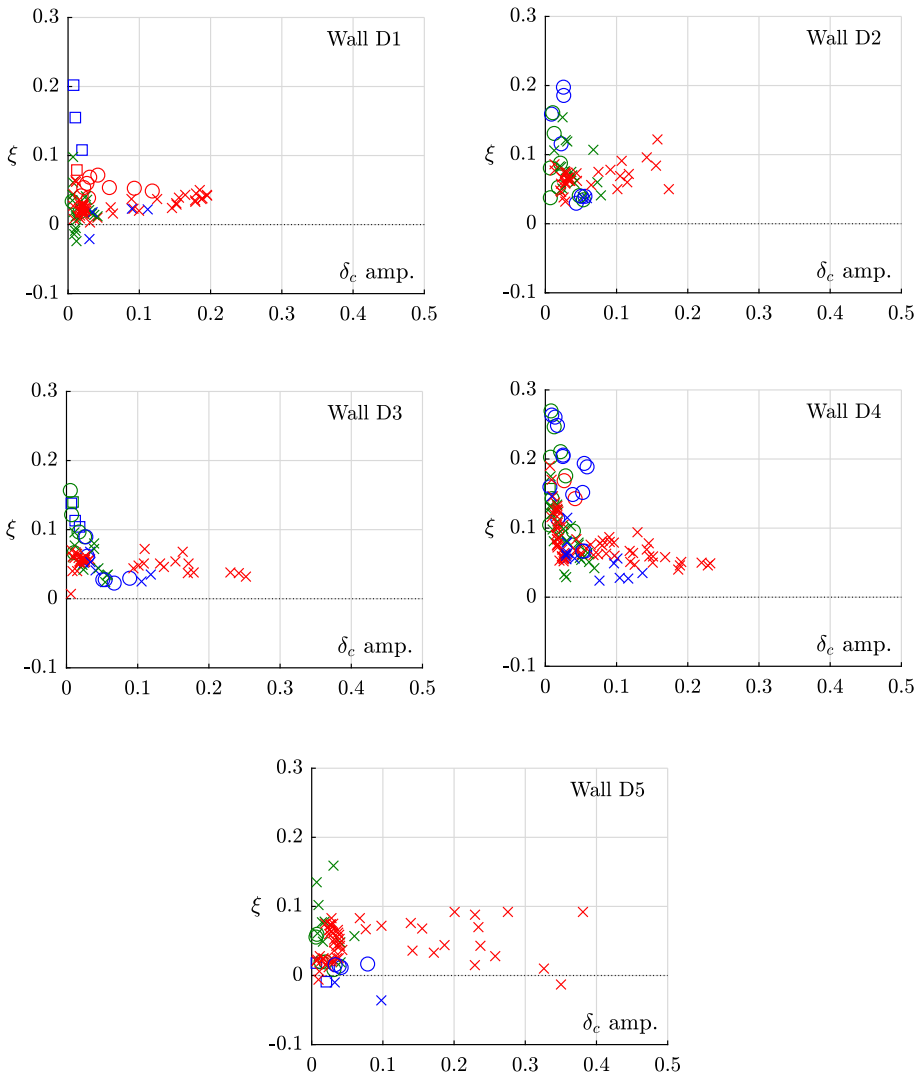


Fig. 10 Hysteretic damping plotted against central displacement amplitude. Data points correspond to the average values of ξ calculated within the peak Δ response range in each test run. Legend provided in Table 3

in Table 5. Notably, the post-cracking load resistance of each wall is still significant compared to the initial peak load (Table 4), in that none of the walls had experienced a significant drop-off in strength. This behaviour can be attributed to rigid body stability and internal friction along the cracked bed joints, which is consistent with findings of the quasistatic cyclic tests.

An unfortunate limitation of the tests undertaken was that due to the capability of the shaketable it was not possible to subject the walls to greater displacements than those that were achieved. The lowest maximum displacement excursion reached across the five tested walls was 13 mm ($\delta = 0.26$) in wall D1, and the largest was 25 mm ($\delta = 0.5$) in wall D5. Consequently the displacement capacity of the walls cannot be deduced from these tests,

but it is worth noting that none of the walls demonstrated any visual signs of being close to destabilisation which is consistent with their a - Δ response (Figs. 8, 9). For reference, rigid body stability predicts the displacement capacity of the walls to range between $\delta = 1.35$ – 1.78 (refer to Sect. 5.2).

A further remarkable feature of the observed F - Δ behaviour is that the walls did not—at least in the range of imposed Δ —exhibit any negative tangent stiffness branches which tend to be indicative of rocking destabilisation as is feature generally associated with vertically spanning walls. Conversely, the cyclic a - Δ response plotted using central acceleration (Fig. 9) consistently displayed excursions with a positive tangent stiffness (n.b. The average acceleration plots in Fig. 8 did exhibit cycles with negative tangent stiffness but this phenomenon is thought to be due to acceleration phase lag along the wall face rather than destabilisation). This behaviour can be partially attributed to the relatively low imposed displacements that were reached in the tests; however, it is also consistent with the quasistatic cyclic tests and can be potentially explained by development of internal arching. The causes of this are thought to include horizontal confinement provided by the vertical edge supports, and/or vertical confinement of the cracks in the vicinity of the return walls. Consequently, the observed response is considered to be a particular characteristic of two-way spanning walls.

4.1.5 Behaviour symmetry in positive and negative displacement

A significant feature of the F - Δ behaviour observed through the quasistatic cyclic tests was the general asymmetry of strength in the positive and negative displacement directions. This was attributed to the large proportion of brick unit line failure along vertical edge cracks and in some cases separation of the main wall from its returns which caused the walls to have a higher post-cracking load resistance when loaded toward the returns. By comparison, the F - Δ response observed in the present tests showed no discernible difference between load resistance in the positive and negative Δ directions—neither before nor after cracking. This more symmetrical response is thought to be due to the fact that stepped failure along the masonry bond was the dominant mode of failure along vertical cracks thus leading to better engagement between the main panel and returns.

4.2 Influence of vertical precompression

Walls with precompression outperformed the corresponding non-loadbearing walls in terms of both their peak strength and post-cracking strength (Tables 4, 5). These trends are consistent with the quasistatic cyclic tests, and can be explained by the enhancement of the flexural and torsional moment capacities along crack lines due to a higher vertical stress.

Comparisons of walls' peak strength need to be treated with caution, due to the fact that in walls without precompression (D2 and D5) the top support is thought to have been ineffective at small displacements, meaning that the walls effectively had only three-sided support when they attained their peak strength (discussed further in Sects. 4.5, 5.1). Nonetheless, if the walls' global peak loads are compared, then the improvement in strength is still evident. For example, between the solid walls, wall D1 with 0.1 MPa precompression (3.25 g) was stronger than the non-loadbearing wall D2 (1.47 g). Interestingly, among the walls with an opening, wall D3 (2.34 g) with 0.1 MPa precompression was slightly weaker than wall D4 (2.44 g) with 0.05 MPa precompression, which could be explained by material strength variability. However both these walls were stronger than the non-loadbearing wall D5 (1.32 g).

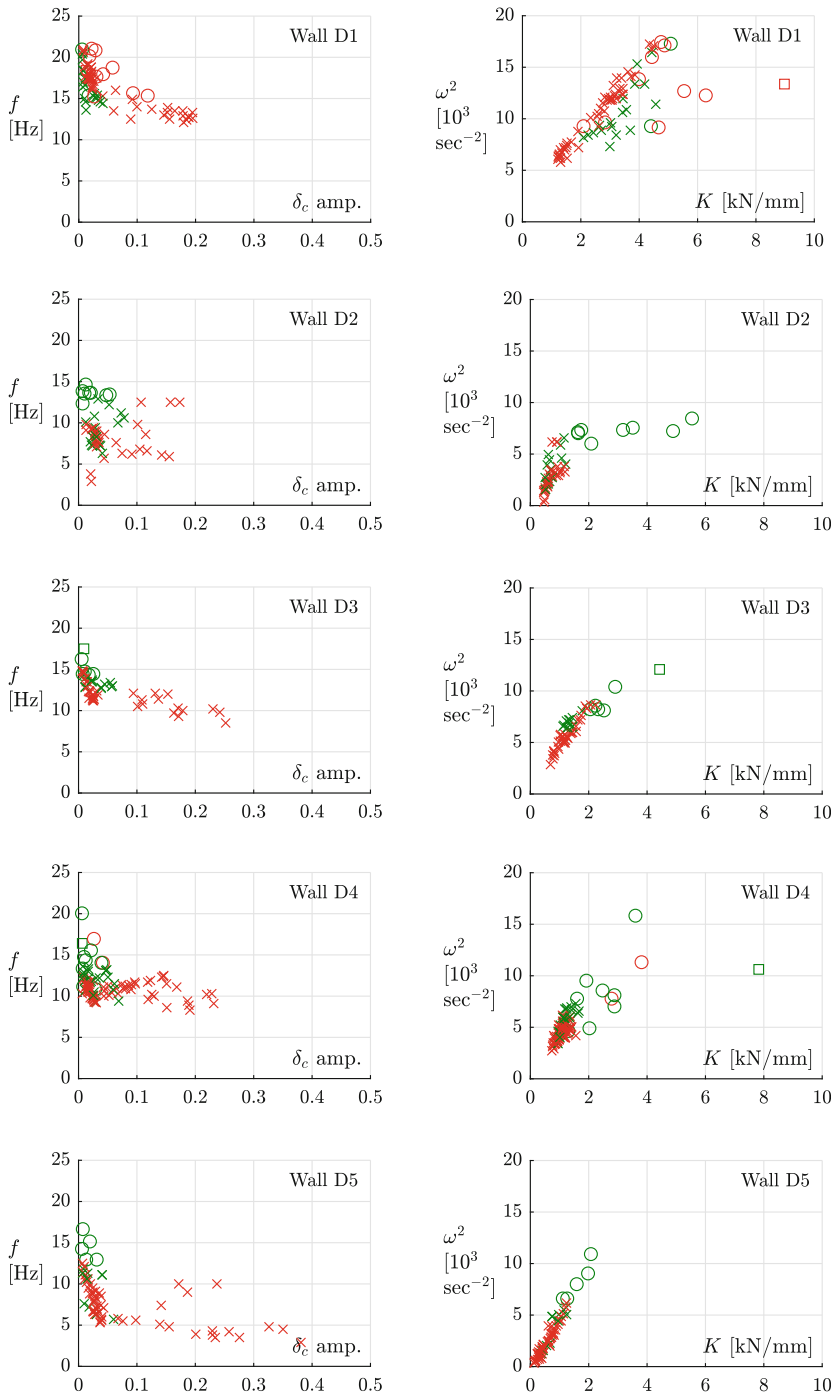


Fig. 11 Free vibration frequency (f) as quantified in individual test runs. Graphs on the left side show the frequency versus central displacement δ_c . Graphs on the right side plot the square of the angular frequency (where $\omega = 2\pi f$) versus effective stiffness K calculated using the wall’s central acceleration. Legend provided in Table 3

A similar enhancement in strength is observed by considering the post-cracking strength of the corresponding set of walls at a reference displacement of $\delta = 0.2$ (Table 5). For example, wall D1 with 0.10 MPa precompression has 20% higher strength than the non-loadbearing wall D2. Similarly among the walls with an opening, walls D3 and D4 (0.1 and 0.05 MPa precompression) have, respectively, 90 and 40% higher strength than the non-loadbearing wall D5.

4.3 Hysteretic damping

Hysteretic damping (ξ) was quantified using the walls' central acceleration hysteresis response (curves in Fig. 9) as per Eq. (9). The resulting values of ξ are plotted versus the cycle Δ amplitude in Fig. 10 for each wall.

Due to the typically irregular shape of the experimental hysteresis loops, the computed values of ξ exhibit considerable scatter which is most prominent at small displacement ($\delta < 0.05$) but reduces at increased displacement. In the largest range of imposed displacements ($\delta = 0.10$ – 0.30), the measured damping lies within approximately $\xi \approx 0.02$ – 0.10 for every wall. The observed damping is a consequence of frictional resistance mechanisms along cracked bed joints which is characteristic of the flexural response of two-way spanning walls.

For comparison, in the quasistatic cyclic tests hysteretic damping was measured to be between $\xi \approx 0.09$ – 0.15 over the same range of normalised displacement ($\delta = 0.10$ – 0.30). The associated F - Δ curves along with plots of ξ are provided in “Appendix 2” (Fig. 17). The slight difference in the measured hysteretic damping between the two studies could potentially be explained by the different types of brick units used to construct the walls—the current shaketable study used solid brick units, whilst the quasistatic cyclic tests used 10-hole perforated brick units. It is likely that the latter type of units created better interlock between the bricks and mortar, thus giving rise to higher effective friction and greater energy dissipation under cyclic loading. However, the measured damping is also likely to have been influenced by scaling effects and therefore comparisons to the full-scale walls should be treated as indicative only.

4.4 Vibrational frequency

The left-hand side of Fig. 11 plots the walls' free vibration frequency ($f = 1/T$) versus displacement amplitude (δ_{amp}) as computed in individual test runs. Despite considerable scatter, the plots demonstrate a reduction in frequency with increasing levels of imposed displacement which is indicative of the walls' progressive softening due to damage.

The plots further demonstrate that once fully-cracked, walls with precompression had a higher vibrational frequency than the corresponding non-loadbearing walls. For example at the reference displacement $\delta = 0.15$, the frequencies of solid walls D1 (0.1 MPa) and D2 (no precomp.) are approximately 13 and 9 Hz respectively, whilst walls D3 (0.1 MPa), D4 (0.05 MPa) and D5 (no precomp.) with openings have frequencies of approximately 11, 10 and 6 Hz respectively. This can be explained by the higher post-cracking load resistance and therefore stiffness in walls with precompression.

An approximately linear trend becomes observed for each wall when the square of the angular frequency ($\omega = 2\pi f$) is plotted against the secant stiffness K , as shown on the right-hand side of Fig. 11. This behaviour is consistent with the fundamental relationship $\omega = K/M$, where M is the effective mass of the system. Back-calculating the effective mass M using the experimentally measured values of ω with K computed using the average

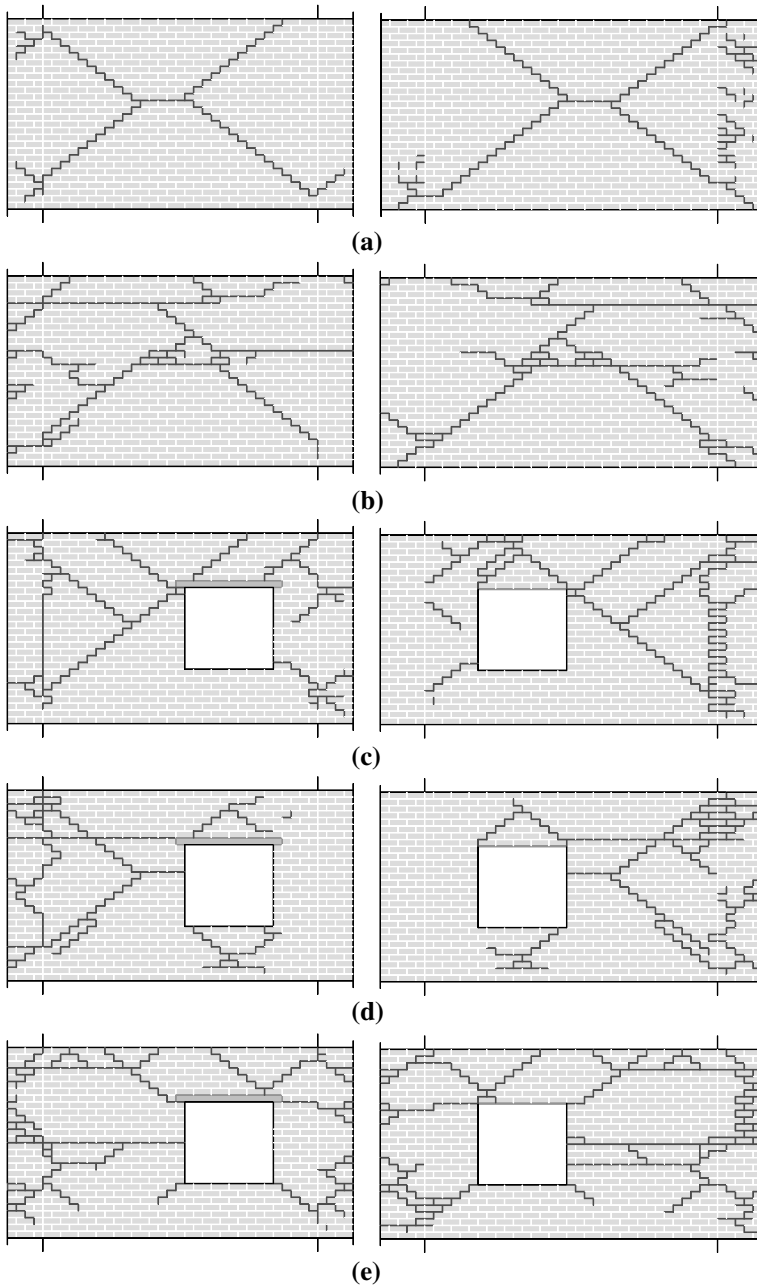


Fig. 12 Cracking patterns at the conclusion of testing. The left and right hand side diagrams show the inside and outside faces of each wall, respectively. Note that the illustrations show the unfolded view of the walls including returns. **a** Wall D1 ($\sigma_{vo} = 0.10$ MPa), **b** wall D2 ($\sigma_{vo} = 0$ MPa), **c** wall D3 ($\sigma_{vo} = 0.10$ - MPa), **d** wall D4 ($\sigma_{vo} = 0.05$ MPa) and **e** wall D5 ($\sigma_{vo} = 0$ MPa)

acceleration gives mass within the range 50–200 kg, which is comparable to the expected effective single-degree-of-freedom wall mass. For comparison, the net actual mass of the walls was 245 kg (D1–D2) and 212 kg (D3–D5). The scatter in the back-calculated effective mass can be partially explained by the inherent approximation in using the wall's recorded Δ response waveform to estimate its free vibration frequency, since the response will naturally retain some of the original frequency content of the input motion.

4.5 Observed damage

4.5.1 Cracking patterns

The cracking patterns exhibited by each wall at the conclusion of testing are shown in Fig. 12. Photographs of wall D3 are provided in Fig. 13 which is considered indicative of the degree of damage that the all walls underwent during the course of testing.

The shapes of the cracking patterns are generally consistent with collapse mechanisms associated with two-way spanning URM walls under biaxial bending, which are characterised by diagonal cracks that propagate inward from corners where laterally supported edges intersect each other (Fig. 12). Such mechanisms are embodied in various adaptations of the rigid plastic approach used for predicting the ultimate load capacity of URM walls under biaxial bending, including methods prescribed by Eurocode 6 (European Committee for Standardisation 2005), the Australian code AS 3700 (Standards Australia 2011; Lawrence and Marshall 2000), as well as various other methods (e.g., Sinha 1978; Baker et al. 2005). Notably the cracking patterns are also consistent with those observed in the quasistatic cyclic tests which are provided in “Appendix 2” for reference (Fig. 16).

Whilst the observed and idealised cracking patterns are in general agreement, the following deviations from expected behaviour can be observed:

- Wall D2 (Fig. 12b) failed to develop top diagonal cracks as would be expected for a wall with its top edge supported (Fig. 14a). Instead, the developed pattern exhibits a series of short diagonal cracks which can together be considered to form an overall vertical crack from approximately the centre of the wall to the top edge. The resulting pattern is similar to that of a wall with a free top edge (Fig. 14c).
- Similarly, wall D5 (Fig. 12e) also failed to develop a top diagonal crack in its longer panel, which would be expected since the top edge was supported (Fig. 14b).

That the above was only observed in the two walls without precompression suggests that in the absence of precompression the top edge support may have been ineffective at low displacements. This could have been either due to a gap between the wall and supporting angle member or the flexibility of the intermediate rubber bearing (Fig. 3a). Interestingly, theoretical predictions of ultimate strength reported in Sect. 5.1 are consistent with this explanation. It is emphasised however that the observed discrepancy with respect to expected behaviour is deemed to be a result of the experimental arrangement used and does not affect the general findings of this study.

4.5.2 Cracks along vertical edges

Due to the moment fixity provided along vertical edges, vertical cracks were generated to a different degree along the vertical edges of each of the specimens (Fig. 12). These cracks became fully developed in walls D3, D4 and D5, but only partially developed in walls D1 and D2 where they did not extend along the full height of the wall.



Fig. 13 Wall D3 at the conclusion of testing

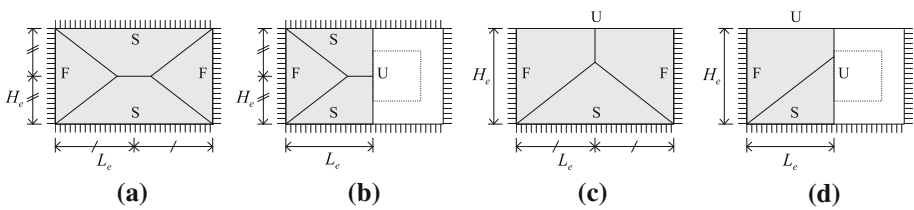


Fig. 14 Idealised collapse mechanisms. Edge restraint conditions are denoted as: *S* simple pinned support, *F* fixed support, *U* unsupported

In each wall, vertical cracks developed exclusively by the mechanism of stepped failure (along mortar joints) as opposed to line failure (rupture of brick units). Stepped failure leads to more favourable seismic performance, as the resulting cracks can maintain a residual moment capacity by friction and therefore facilitate two-way action even after the formation of a full collapse mechanism. In contrast, the walls in the quasistatic cyclic test study developed approximately equal amounts of stepped and line failure along their vertical edges and in some instances localised concentrations of line failure caused separation of the main wall from its returns. The difference in the dominant mode of vertical cracking observed in the two studies is a consequence of the relative strength of the brick units and masonry bond, which can be treated using a probabilistic analytical approach described in Vaculik and Griffith (2017b).

It is thought that the fact that only stepped failure was observed in the present tests contributed favourably toward the behaviour that was observed. Therefore, it would be of additional research value to perform shaketable tests on walls built with masonry more susceptible to line failure, as such walls would be expected to perform more poorly than those in the present study.

It is further worth noting that although frictional sliding along the stepped vertical cracks could still lead to disengagement of the main wall from its return walls, such a failure mode was prevented in walls D1 and D2 by the restraint arrangement implemented; i.e. timber walers stopping outward movement of the returns (Figs. 2, 3b). However even in walls D3–D5, which did not incorporate the waler detail, frictional interlock was still shown to be sufficient to avoid separation of the main wall from its returns even though some minor sliding was observed.

4.5.3 Lateral sliding between panels

Localised out-of-plane sliding between the successive courses of neighbouring subpanels was observed—to various degrees—in each of the walls tested. The two solid walls (D1 and D2) exhibited the most severe cases of such behaviour whereby the maximum slip between adjacent panels was measured to be approximately 20 mm (40% of the wall thickness). The resulting reduction in the bearing area between the panels is thought to have partially contributed to the degradation in the walls' F - Δ behaviour.

Similar cases of sliding between neighbouring subpanels were also observed in the quasistatic cyclic tests but to a lesser degree, which is thought to be partly due to the confinement provided by the airbags on both sides of the wall. Nonetheless, whilst the slip observed in the current tests was in some cases significant, it only occurred during the latter stages of testing at which point the walls had undergone an atypically large number of deformation cycles—well in excess of the number of cycles expected in realistic earthquake motions. Therefore the behaviour observed in the present tests is deemed to be in reasonable agreement with conditions imposed in the quasistatic cyclic tests. However this view should be further validated through future shaketable testing in which the test walls can be subjected to larger deformation cycles closer to those imposed in the quasistatic tests (with δ approaching 1).

5 Comparison with theoretical predictions

In this section the experimental a - Δ response in Fig. 8 is compared with predictions of simplified rigid-plastic techniques that utilise the idealised collapse mechanisms shown in Fig. 14. Implicit in each set of predictions is the assumption that a uniform inertial load is applied to the wall.

5.1 Ultimate strength

The general framework of the virtual work method as developed by Lawrence and Marshall (2000) was used to predict the ultimate wall strength making allowance for the flexural tensile strength of the masonry.

The method begins with the assumption of an idealised collapse mechanism and proceeds to solve for the ultimate load by equating the external work performed by the applied load to the internal work generated along the rotating hinge lines. Included in the internal work term are moment contributions from vertical cracks (horizontal bending moment) and diagonal bending, but contributions from horizontal cracks are ignored on the rationale that they crack early in the response and do not contribute to the peak load resistance. A further assumption is that the slope of diagonal cracks is pre-determined from the basic geometry of the brick unit and mortar joint as shown in Fig. 15, and is thus obtained as follows:

$$G = \frac{2(h_u + t_j)}{l_u + t_j} \tag{10}$$

where, as shown in Fig. 15, h_u = height of brick unit, l_u = length of brick unit, t_j = thickness of mortar joint. Thus, for the tested masonry h_u = 39 mm, l_u = 110 mm, and t_j = 5 mm.

Notably, this general approach has been codified in the Australian masonry code AS 3700; however, the method used here differs in that it uses alternate, more robust analytical expressions for calculating the ultimate moment capacities. These revised expressions are based on work in Willis et al. (2004) and Griffith et al. (2005) which have been later modified in Griffith and Vaculik (2007) and Vaculik and Griffith (2017b).

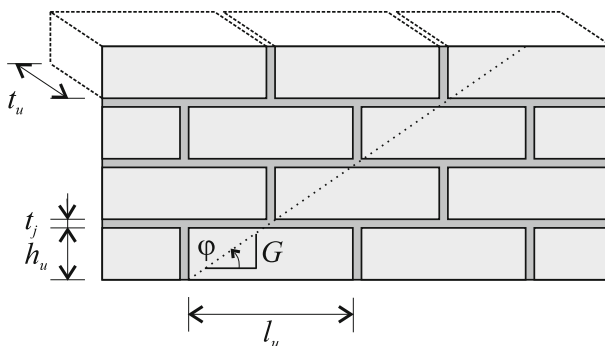


Fig. 15 Fundamental geometric properties in half-overlap masonry

The moment capacity in horizontal bending (M_h) is taken as the lesser of stepped and line failure capacities as follows:

$$M_h = \frac{1}{2(h_u + t_j)} \times \text{lesser of} \left\{ \begin{array}{l} \tau_{um} k_{be} t_u^3 \\ \frac{1}{2} (f_{ur} - \nu_u f_d t_u^2 / 6) \end{array} \right. \quad (11)$$

where t_u = thickness of brick unit (equal to 50 mm), f_{ur} = modulus of rupture of brick unit, f_d = acting vertical stress at the crack, ν_u = Poisson’s ratio of brick unit taken as 0.2, k_{be} = elastic torsion constant equal to 0.208 for a square bed joint overlap, and τ_{um} = torsional shear stress capacity taken as

$$\tau_{um} = 1.6f_{mt} + 0.9f_d, \quad (12)$$

where f_{mt} = flexural tensile strength of the masonry, and all other variables as defined previously. The τ_{um} -proportional term in Eq. (11) represents the resistance against stepped failure, which is taken as the elastic torsional capacity of the rectangular bed joint section having the dimensions t_u by $(l_u - t_j)/2$ (Vaculik and Griffith 2017b). The f_{ur} -based term in Eq. (11) is the resistance against line failure, whose capacity is derived from the flexural rupture strength of the brick unit. Notably, the contributions of perpend are ignored in both equations.

The moment capacity in diagonal bending (M_d) is taken as

$$M_d = \frac{\sin \varphi}{h_u + t_j} \left[(\sin \varphi)^3 \tau_{um} k_{be} t_u^3 + (\cos \varphi)^3 (f_{mt} + f_d) (l_u + t_j) t_u^2 / 12 \right] \quad (13)$$

where φ = angle of diagonal crack taken as $\arctan(G)$, and all other variables as defined previously. Equation (13) is based on the premise that the moment capacity along a diagonal crack is derived from a combination of the torsional and flexural capacity of the bed joints with the assumption of a linear interaction between these two sources of resistance (Griffith et al. 2005; Griffith and Vaculik 2007).

The described approach was applied to the five tested walls D1-D5 using mean measured value of f_{mt} as given in Table 1, and similarly to the five corresponding full scale walls in the quasistatic test study.

Solid walls (D1 and D2) were analysed by applying the full four-sided mechanism (Fig. 14a), whereas walls with an opening (D3-D5) were analysed by considering only the longer side panel and treating the edge of the opening as a free edge (Fig. 14b). For comparison, walls without precompression (D2 and D5) were also considered by treating the top edge as unsupported (Fig. 14c, d). In each analysis, the vertical edge cracks were assumed to contribute only 50% of their horizontal moment capacity. This assumption was found previously to produce good correlation with the ultimate load of the quasistatic cyclic test walls on the basis that only a proportion of their moment capacity is active at the point of peak load (Griffith and Vaculik 2007), and can be justified by the fact that the walls had identical boundary conditions along these edges in both studies.

For walls D1-D5, the theoretical predictions are superimposed onto the experimental a - Δ capacity curves in Fig. 8. Results for the quasistatic cyclic test walls provided in “Appendix 2” (Figure 17). The following observations are made regarding the accuracy of the method:

- Comparison between the peak experimental loads and predictions made using the four-sided mechanisms is favourable for each of the walls with precompression (D1, D3 and D4).
- In the two walls without precompression (D2 and D5), the four sided mechanism overpredicts the initial peak even though it happens to agree quite well with the second peak in wall D2. However, the three-sided mechanism compares well with initial peak in both walls. This further supports that the top edge support was likely to have been ineffective as discussed earlier.
- The approach produces equally good correlation with the quasistatic cyclic test walls, indicating that the behaviour of walls in both sets of tests is consistent when compared to the theoretical predictions as a benchmark despite any effects due to scaling.
- Differences between the experimental and predicted values of strength are deemed to be well within the bounds of material strength variability (COV of $f_{m1} = 0.53$).

5.2 Post-cracking capacity

The theoretical post-cracking capacity envelope of each wall was constructed using an approach proposed by Vaculik and Griffith (2017a) in which the total resistance is taken as the superposition of contributions from rocking and inelastic friction. By assuming the wall to be already-cracked, the approach includes resistance sources provided solely from gravity and thus ignores any contributions from tensile strength. It furthermore treats the wall as rigid-plastic and does not incorporate an initial linear-elastic loading branch.

As was the case with the prediction of ultimate strength described in Sect. 5.1, this technique requires an initial assumption of a collapse mechanism—for this, all tested walls were analysed by assuming the top edge to be restrained, since in walls D2 and D5 the top support must become engaged at large central wall displacement. Thus walls D1 and D2 were analysed using the mechanism shown in Fig. 14a, and walls D3–D5 using the mechanism in Fig. 14b. The associated capacities of these mechanisms were calculated using the following mechanics-based expressions. For additional detail regarding these expressions including the process used to derive them the reader is referred to Vaculik and Griffith (2017a).

The rocking component of the force–displacement response is treated as linear-descending and is therefore defined by its load and displacement capacities, λ_{ro} and δ_{ro} . Expressions for these capacities were derived in Vaculik and Griffith (2017a) by considering rigid-body stability mechanics of the sub-panels involved in the overall mechanism, which for the mechanisms shown in Fig. 14a, b are as follows:

$$\lambda_{ro} = \frac{t_u}{H_t} \cdot \frac{3/2 - a/2 + 2\psi(1 - a\epsilon)}{2/3 + a/3} \quad (14)$$

and

$$\delta_{ro} = \frac{3/2 - a/2 + 2\psi(1 - a\epsilon)}{2/3 + a/3 + \psi(1 + a)} \quad (15)$$

where H_t = full height of the mechanism, ψ = normalised precompression defined as $\sigma_{vo}/(\gamma H_t)$, ϵ = precompression eccentricity parameter taken as 0.5 for a concentric load, and a is a geometric parameter calculated as follows:

$$a = 1 - 1/\alpha \quad (16)$$

$$\alpha = GL_e/H_e \text{ with } H_e = H_t/2 \quad (17)$$

where L_e = effective mechanism length, which is taken as half of the total length of the mechanism shown in Fig. 14a, or the length from the supported vertical edge to the edge of the opening in the mechanism shown in Fig. 14b. All other variables are as defined previously.

The load capacity of the inelastic component from torsional friction in horizontal bending is calculated as

$$\lambda_{ho} = \frac{\mu_m k_{bp} t_u^2}{h_u + t_j} \cdot \frac{G}{L_e} \cdot \frac{R_{vs}(1 + 2\psi)}{2/3 + a/3} \quad (18)$$

where μ_m = friction coefficient (taken as 0.576, refer Table 1), k_{bp} = plastic torsion coefficient (0.383 for square overlap), R_{vs} = vertical edge restraint factor (taken as 1 for full moment fixity), and other variables as defined previously. Equation (18) was derived in Vaculik and Griffith (2017a) using a virtual work approach that is conceptually identical to that described in Sect. 5.1; however it uses the plastic torsion coefficient k_{bp} (instead of k_{be}) which assumes a fully-plasticised distribution of frictional shear stress along the bed joint section.

Note that the above Eq. (14)–(18) are only applicable to mechanism geometries where $\alpha \geq 1$. For mechanism geometries outside this range the reader is referred to Vaculik and Griffith (2017a).

The resulting theoretical capacity envelopes are plotted in Fig. 8 for the initial rocking component (λ_{ro}) and for combined rocking plus inelastic strength ($\lambda_{ro} + \lambda_{ho}$). The following observations are made about the accuracy of the method:

- The predicted theoretical capacity envelopes provide conservative estimates of the walls' post-cracked strength.
- Due to the rising branches observed in the actual behaviour, experimental excursions begin to exceed the theoretical envelope above $\delta > 0.2$ in wall D3 and $\delta > 0.1$ in the remaining walls. These rising branches are thought to be due to internal arching effects which are not captured in the model.
- The method is particularly conservative in the walls without precompression since it treats load capacity as directly proportional to the axial stress in the wall.

The above observations are consistent in relation to both the shaketable test walls and quasistatic cyclic teste walls.

6 Concluding remarks

This paper has described shaketable tests on five half-scale, two-way spanning URM walls. The wall configurations emulated walls subjected to quasistatic cyclic loading in a previous study by the authors (Griffith et al. 2007) with the intent of verifying whether the response could be reproduced under true dynamic inertial loading. The tests performed validated the most significant wall behaviour characteristics observed in the original study, as follows.

- The initial peak load capacity was reached at small displacements during the initial sequence of cracking accompanied by the development of a two-way bending failure mechanism.
- Even after becoming fully cracked the walls maintained substantial residual strength due to internal flexure and torsion along the cracked bed joints. As a result of equipment limitations, the imposed displacement levels were low compared to those reached in the quasistatic cyclic tests. Whilst it was not possible to quantify the displacement capacity of the walls, none of the walls had demonstrated any obvious signs of approaching collapse.
- Under cyclic loading the measured $F-\Delta$ behaviour displayed significant hysteretic energy dissipation due to the frictional resistance associated with two-way bending.
- Strength and stiffness degradation occurred as a result of damage accumulation with increasing displacement excursions and number of cycles.
- The observed damage and cracking pattern shapes were in good agreement with collapse mechanisms associated with walls under biaxial bending.
- The measured strength in both sets of studies agreed well with the ultimate load capacity predicted using a simplified virtual work approach. By comparison, theoretical predictions of the post-cracking strength were conservative with reference to both sets of tests.

The tests also demonstrated some aspects of behaviour that were not as prominent in the quasistatic cyclic tests, in particular the following:

- After becoming fully cracked some of the walls exhibited considerable lateral sliding between their neighbouring subpanels in the out-of-plane direction. The severity of the sliding however was not sufficient to cause any local collapse through a loss of bearing. Whilst the airbag arrangement used in the quasistatic cyclic tests was likely to have mitigated such behaviour in that study, in the present tests this behaviour occurred only after the walls were subjected to a very large number of cycles.
- Stepped failure was the exclusive mode of failure that occurred along the rotationally and laterally restrained vertical edges. This was a result of the mechanical properties of the masonry used to build the walls, in particular the high flexural strength of the brick units relative to the bond. Stepped cracks are preferable to line cracks with respect to seismic performance and may have contributed to the favourable behaviour observed.

It would be of additional research value to supplement the present work with further future testing, particularly using masonry that is more susceptible to line failure along the vertical supported edges, as well as to generate larger levels of imposed displacement in order to quantify the walls' displacement capacities.

Acknowledgements This research was conducted with the financial support of the Australian Research Council (Grant No. DP0450933) and The University of Adelaide. The technical assistance of staff from the School of Civil, Environmental and Mining Engineering is also gratefully acknowledged.

Appendix 1: Supplementary material

Supplementary material can be found online at the following DOI:

<http://doi.org/10.4225/55/5a0138124b6c0>

The material provided consists of two files. The first is a document (120 pages) containing additional detail relating to these tests, including:

- Material test methods and results,
- Test run naming convention,
- Earthquake input motions,
- Basic data processing,
- Cyclic response analysis,
- Data filtering,
- Force-displacement graphs,
- Cracking pattern photographs, and
- Description of attached data (unprocessed and processed).

The second file is a ZIP file containing unprocessed and processed time-domain data for each of the test runs undertaken.

Appendix 2: Results of quasistatic cyclic tests (Griffith et al. 2007)

The purpose of this appendix is to provide selected results of the quasistatic cyclic test study reported in Griffith et al. 2007 as a reference for comparison of the results observed in the present tests.

Only walls S1–S5 from the quasistatic cyclic test study are considered here as they are the full-scale equivalents of the half-scale test walls D1–D5 tested in the present study. The reader is referred to the original paper for additional information including material properties, test procedure, and results for the remaining three walls (S6–S8).

Cracking patterns

Cracking patterns exhibited by walls S1–S5 at the conclusion of testing are shown in Fig. 16.

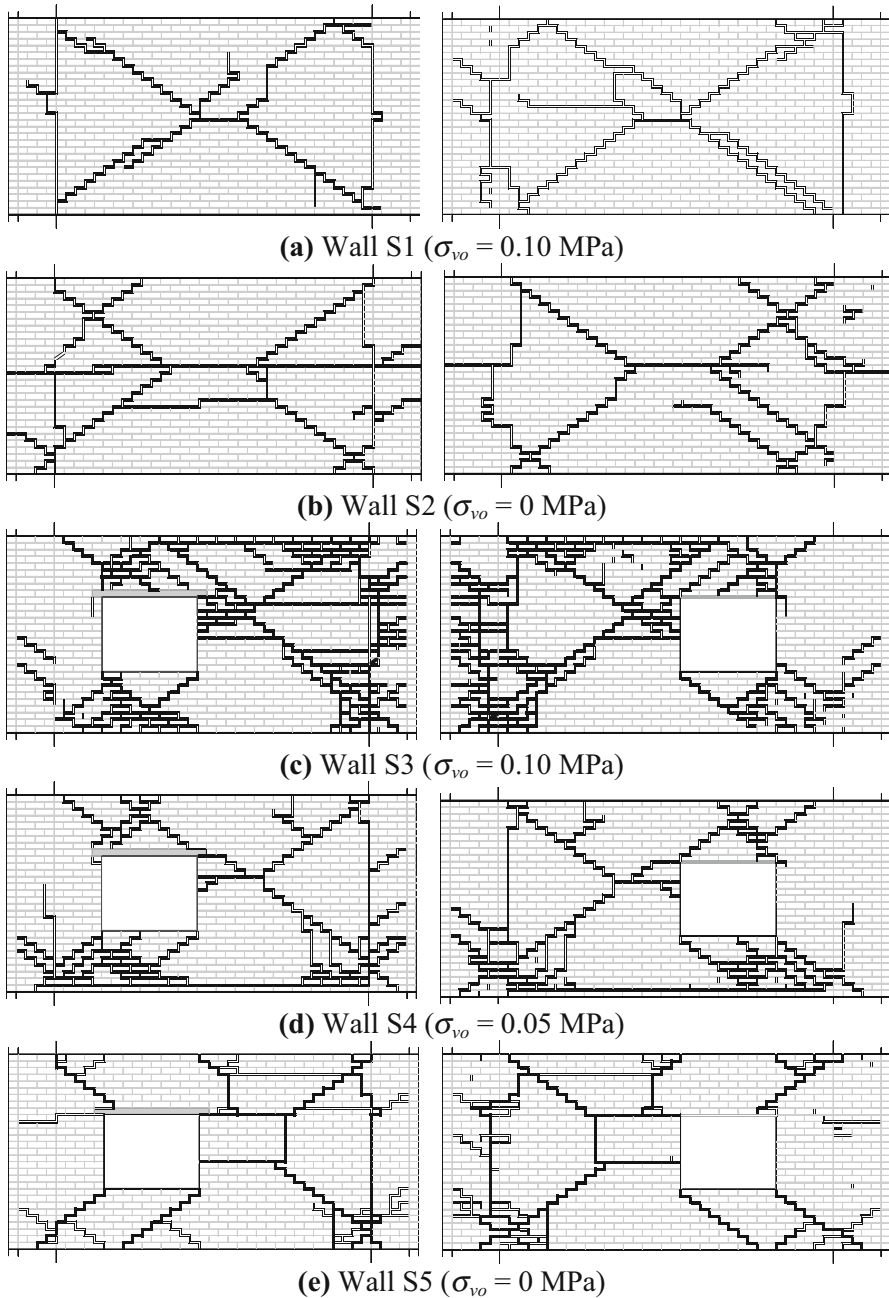


Fig. 16 Cracking patterns at the conclusion of quasistatic cyclic tests as reported in Griffith et al. 2007. The illustrations show an unfolded view of the walls including returns. Severe exhibiting a higher degree of damage or spalling cracks are highlighted as thick lines whilst cracks with lesser damage are shown as thin lines. Graphics remain copyright of John Wiley & Sons, Ltd. (2006); used with permission from Wiley. **a** Wall S1 ($\sigma_{vo} = 0.10$ MPa), **b** Wall S2 ($\sigma_{vo} = 0$ MPa), **c** Wall S3 ($\sigma_{vo} = 0.10$ MPa), **d** Wall S4 ($\sigma_{vo} = 0.05$ MPa) and **e** Wall S5 ($\sigma_{vo} = 0$ MPa)

F-Δ capacity curves

Figure 17 provides for each wall S1–S5 a plot of the $F-\Delta$ behaviour as well as hysteretic damping ratio (ξ) computed using the same approach as in the present study [refer Eq. (9)].

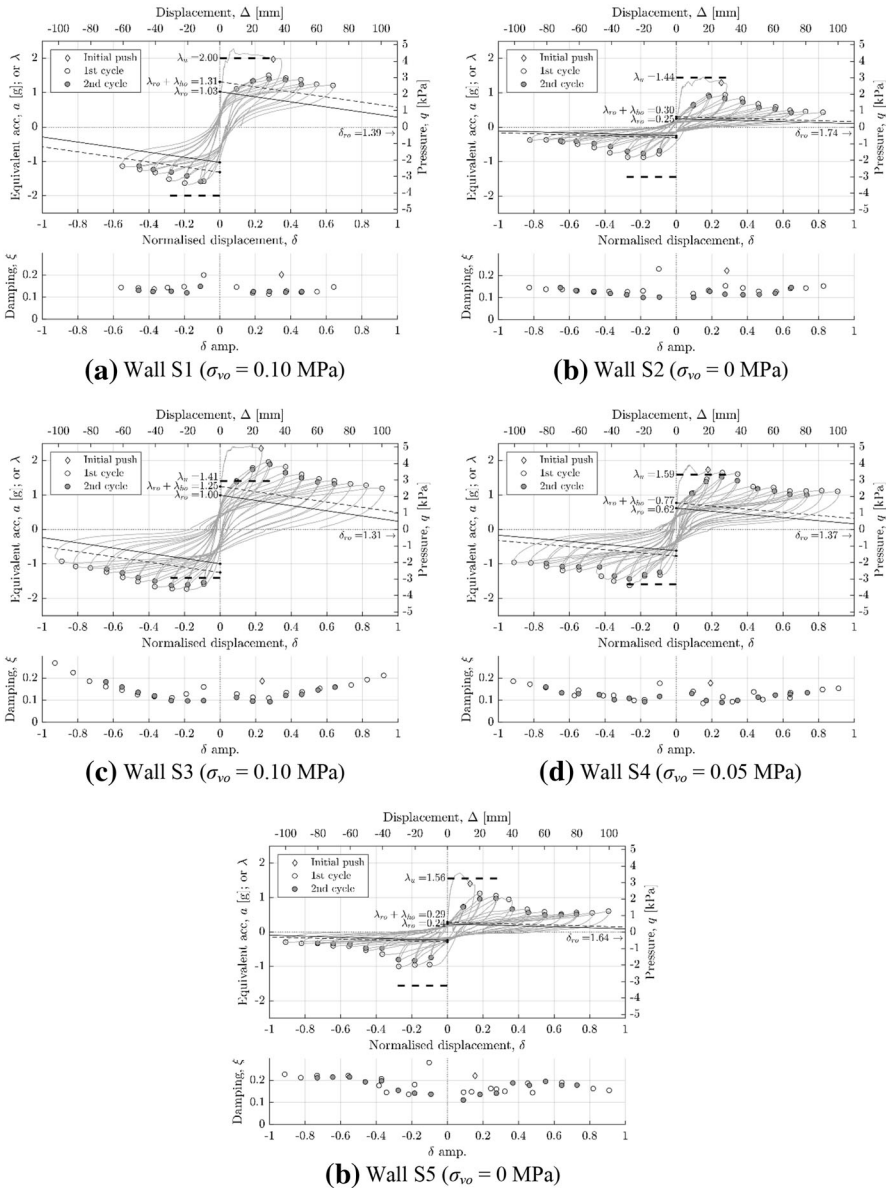


Fig. 17 $F-\Delta$ behaviour and hysteretic damping for quasistatic cyclic test walls S1–S5 as reported in Griffith et al. 2007. Also shown are analytical capacity predictions including: ultimate strength λ_u (thick dashed line), residual strength from rigid body rocking λ_{ro} (thin solid line, x-intercept at δ_{ro}), and residual strength inclusive of horizontal bending friction $\lambda_{ro} + \lambda_{ho}$ (thin dashed line). **a** Wall S1 ($\sigma_{vo} = 0.10$ MPa), **b** Wall S2 ($\sigma_{vo} = 0$ MPa), **c** Wall S3 ($\sigma_{vo} = 0.10$ MPa), **d** Wall S4 ($\sigma_{vo} = 0.05$ MPa) and **e** Wall S5 ($\sigma_{vo} = 0$ MPa)

For reference, the predicted load capacities calculated using the analytical techniques described in Sect. 5 are also plotted.

References

- Abrams D (1996) Effects of scale and loading rate with tests of concrete and masonry structures. *Earthq Spectra* 12(1):13–28
- Al Shawa O, de Felice G, Mauro A, Sorrentino L (2012) Out-of-plane seismic behaviour of rocking masonry walls. *Earthq Eng Struct Dyn* 41(5):949–968
- Baker C, Chen B, Drysdale R (2005) Failure line method applied to walls with openings. In: Proceedings of 10th Canadian masonry symposium, Banff, Alberta, Canada
- Benedetti D, Carydis P, Pezzoli P (1998) Shaking table tests on 24 simple masonry buildings. *Earthq Eng Struct Dyn* 27(1):67–90
- Beyer K, Tondelli M, Petry S, Peloso S (2015) Dynamic testing of a four-storey building with reinforced concrete and unreinforced masonry walls: prediction, test results and data set. *Bull Earthq Eng* 13(10):3015–3064
- Bothara JK, Dhakal RP, Mander JB (2010) Seismic performance of an unreinforced masonry building: an experimental investigation. *Earthq Eng Struct Dyn* 39(1):45–68
- Calvi GM, Kingsley GR, Magenes G (1996) Testing of masonry structures for seismic assessment. *Earthq Spectra* 12(1):145–162
- Costa AA, Arede A, Costa A, Oliveira CS (2012) Out-of-plane behaviour of existing stone masonry buildings: experimental evaluation. *Bull Earthq Eng* 10(1):93–111
- Costa AA, Arede A, Costa AC, Penna A, Costa A (2013) Out-of-plane behaviour of a full scale stone masonry facade. Part 2: shaking table tests. *Earthq Eng Struct Dyn* 42(14):2097–2111
- Dafnis A, Kolsch H, Reimerdes HG (2002) Arching in masonry walls subjected to earthquake motions. *J Struct Eng* 128(2):153–159
- D’Ayala DF, Paganoni S (2011) Assessment and analysis of damage in L’Aquila historic city centre after 6th April 2009. *Bull Earthq Eng* 9(1):81–104
- D’Ayala D, Shi Y (2011) Modeling masonry historic buildings by multi-body dynamics. *Int J Archit Herit* 5(4–5):483–512
- D’Ayala D, Speranza E (2003) Definition of collapse mechanisms and seismic vulnerability of historic masonry buildings. *Earthq Spectra* 19(3):479–509
- de Felice G, Giannini R (2001) Out-of-plane seismic resistance of masonry walls. *J Earthq Eng* 5(2):253–271
- Derakhshan H, Griffith MC, Ingham JM (2013) Airbag testing of multi-leaf unreinforced masonry walls subjected to one-way bending. *Eng Struct* 57:512–522
- European Committee for Standardisation (2005) Eurocode 6, design of masonry structures—part 1–1: general rules for reinforced and unreinforced masonry structures. CEN, Brussels
- Ewing RD, Kariotis JC (1981) Methodology for mitigation of seismic hazards in existing unreinforced masonry buildings: wall testing, out-of-plane. Technical Report. ABK-TR-04, ABK, a joint venture, El Segundo, California
- Graziotti F, Tomassetti U, Penna A, Magenes G (2016) Out-of-plane shaking table tests on URM single leaf and cavity walls. *Eng Struct* 125:455–470
- Griffith MC, Vaculik J (2007) Out-of-plane flexural strength of unreinforced clay brick masonry walls. *TMS J* 25(1):53–68
- Griffith MC, Lam NTK, Wilson JL, Doherty K (2004) Experimental investigation of unreinforced brick masonry walls in flexure. *J Struct Eng* 130(3):423–432
- Griffith MC, Lawrence SJ, Willis CR (2005) Diagonal bending of unreinforced clay brick masonry. *Mason Int* 18(3):125–138
- Griffith MC, Vaculik J, Lam NTK, Wilson J, Lumantarna E (2007) Cyclic testing of unreinforced masonry walls in two-way bending. *Earthq Eng Struct Dyn* 36(6):801–821
- Lagomarsino S (2015) Seismic assessment of rocking masonry structures. *Bull Earthq Eng* 13(1):97–128
- Lawrence SJ (1983) Behaviour of brick masonry walls under lateral loading. Ph.D. thesis, The University of New South Wales
- Lawrence S, Marshall R (2000) Virtual work design method for masonry panels under lateral load. In: Proceedings of 12th international brick and block masonry conference, Madrid, Spain, vol 2, pp 1063–1072

- Lourenço PB, Avila L, Vasconcelos G, Alves JPP, Mendes N, Costa AC (2013) Experimental investigation on the seismic performance of masonry buildings using shaking table testing. *Bull Earthq Eng* 11(4):1157–1190
- Magenes G, Penna A, Senaldi IE, Rota M, Galasco A (2014) Shaking table test of a strengthened full-scale stone masonry building with flexible diaphragms. *Int J Archit Herit* 8(3):349–375
- Meisl CS, Elwood KJ, Ventura CE (2007) Shake table tests on the out-of-plane response of unreinforced masonry walls. *Can J Civil Eng* 34(11):1381–1392
- Moon L, Dizhur D, Senaldi I, Derakhshan H, Griffith M, Magenes G, Ingham J (2014) The demise of the URM building stock in Christchurch during the 2010–2011 Canterbury earthquake sequence. *Earthq Spectra* 30(1):253–276
- Oyarzo-Vera C, Griffith MC (2009) The Mw 6.3 Abruzzo (Italy) earthquake of April 6th, 2009: on site observations. *Bull N Z Soc Earthq Eng* 42(4):302–307
- Page AW (1992) The design, detailing and construction of masonry—the lessons from the Newcastle earthquake. *Trans Inst Eng Aust Civil Eng* 34(4):343–353
- Paquette J, Bruneau M, Filiatrault A (2001) Out-of-plane seismic evaluation and retrofit of turn-of-the-century North American masonry walls. *J Struct Eng* 127(5):561–569
- Penna A, Morandi P, Rota M, Manzini CF, da Porto F, Magenes G (2014) Performance of masonry buildings during the Emilia 2012 earthquake. *Bull Earthq Eng* 12(5):2255–2273
- Penner O, Elwood KJ (2016) Out-of-plane dynamic stability of unreinforced masonry walls in one-way bending: shake table testing. *Earthq Spectra* 32(3):1675–1697
- Portioli F, Casapulla C, Cascini L, D’Aniello M, Landolfo R (2013) Limit analysis by linear programming of 3D masonry structures with associative friction laws and torsion interaction effects. *Arch Appl Mech* 83(10):1415–1438
- Reneckis D, LaFave JM, Clarke WM (2004) Out-of-plane performance of brick veneer walls on wood frame construction. *Eng Struct* 26(8):1027–1042
- Restrepo Vélez LF, Magenes G, Griffith MC (2014) Dry stone masonry walls in bending—part I: static tests. *Int J Archit Herit* 8(1):1–28
- Sinha BP (1978) A simplified ultimate load analysis of laterally loaded model orthotropic brickwork panels of low tensile strength. *Struct Eng* 56B(4):81–84
- Standards Australia (2011) Australian standard for masonry structures (AS 3700–2011). SA, Sydney
- Vaculik J, Griffith MC (2017a) Out-of-plane load-displacement model for two-way spanning masonry walls. *Eng Struct* 141:328–343
- Vaculik J, Griffith MC (2017b) Probabilistic analysis of unreinforced brick masonry walls subjected to horizontal bending. *ASCE J Eng Mech* 143(8):04017056-1-04017056-12
- Vaculik J, Griffith MC, Magenes G (2014) Dry stone masonry walls in bending—part II: analysis. *Int J Archit Herit* 8(1):29–48
- Willis CR, Griffith MC, Lawrence SJ (2004) Horizontal bending of unreinforced clay brick masonry. *Mason Int* 17(3):109–121